

PLANT SCIENCES

The vacuolar K^+/H^+ exchangers and calmodulin-like CML18 constitute a pH-sensing module that regulates K^+ status in Arabidopsis

Miguel Daniel-Mozo^{1†}, Belén Rombolá-Caldentey^{2†}, Imelda Mendoza², Paula Ragel³, Anna De Luca², Raul Carranco², Ana M. Alcaide², Alessio Ausili², Beatriz Cubero⁴, Karin Schumacher³, Francisco J. Quintero², Armando Albert^{1*}, José M. Pardo^{2*}

Shifts in cytosolic pH have been recognized as key signaling events and mounting evidence supports the interdependence between H^+ and Ca^{2+} signaling in eukaryotic cells. Among the cellular pH-stats, K^+/H^+ exchange at various membranes is paramount in plant cells. Vacuolar K^+/H^+ exchangers of the NHX ($Na^+, K^+/H^+$ exchanger) family control luminal pH and, together with K^+ and H^+ transporters at the plasma membrane, have been suggested to also regulate cytoplasmic pH. We show the regulation of vacuolar K^+/H^+ exchange by cytoplasmic pH and the calmodulin-like protein CML18 in Arabidopsis. The crystal structure and physicochemical properties of CML18 indicate that this protein senses pH shifts. Interaction of CML18 with tonoplast exchangers NHX1 and NHX2 was favored at acidic pH, a physiological condition elicited by K^+ starvation in Arabidopsis roots, whereas excess K^+ produced cytoplasmic alkalization and CML18 dissociation. These results imply that the pH-responsive NHX-CML18 module is an essential component of the cellular K^+ - and pH-stats.

INTRODUCTION

The CPA (cation/proton antiporters) superfamily is a group of transmembrane proteins that exchange cations for protons in opposite directions to locally modulate pH, as well as electrical and cation balances. This protein family is fundamental for cellular ion homeostasis and is ubiquitous in organisms across all phyla and kingdoms. The NHX clade of $Na^+, K^+/H^+$ exchangers is present in fungi and the green lineage, from algae to flowering plants (1). The *Arabidopsis thaliana* genome encodes eight NHX homologs, AtNHX1 to AtNHX8. Proteins AtNHX1 to AtNHX4 localize to the vacuolar membrane, AtNHX5 and AtNHX6 reside in other endosomal membranes, and AtNHX7/SOS1 and AtNHX8 are plasma membrane proteins (2, 3). Biochemical characterization of representative members of the intracellular NHXs has shown that they can transport both K^+ and Na^+ , with variable selectivity for the substrate between individual exchangers. While the vacuolar members show similar Na^+/H^+ and K^+/H^+ exchange affinity (4–6), the endosomal proteins present a preference for K^+ over Na^+ as substrate (7, 8). By contrast, AtNHX7/SOS1 is highly selective for Na^+/H^+ exchange, and AtNHX8 has been reported to transport Li^+ (9–12).

Little is known about the signaling pathways that regulate the activity of vacuolar NHX antiporters, but current evidence indicates that both protein phosphorylation and binding of Ca^{2+} /calmodulin are involved. Phosphoproteomic studies in Arabidopsis and rice showed that endosomal NHX antiporters are phosphorylated at their C-terminal tails (13) although the physiological role has not

yet been resolved. Phosphorylation of the apple (*Malus domestica*) MdNHX1 at Ser²⁷⁵ by glucose hexokinase1 (MdHCK1) improved protein stability and enhanced activity of MdNHX1 (14). On the other hand, CML18 is known to interact with AtNHX1 and modulate $Na^+, K^+/H^+$ exchange (15, 16), but whether this interaction was essential for AtNHX1 activity and if CML18 interacted with other family members has remained unknown. Moreover, the physiological context of this interaction has been circumscribed to the salinity stress response and Na^+ accumulation into vacuoles. However, further research has shown the essential role of tonoplast NHXs in the vacuolar storage of K^+ for nutrition, osmotic adjustment, cell expansion, stomatal movements, and the control of luminal pH (5, 17, 18). Here, we show that NHX-CML18 interaction responds primarily to cytosolic acidification elicited by K^+ limitation.

Cation/proton exchangers catalyze the countertransport of acid-base equivalents, and thus, they are critical for pH regulation. Endosomal NHX proteins couple their activity to the H^+ electrochemical gradient maintained by H^+ pumps, and thus, they serve as proton leaks to regulate the luminal pH of endosomes (18–20). However, considering the large volume of plant vacuoles, tonoplast-localized NHXs could also play a substantial role in buffering and responding to fluctuations in the cytosolic pH. The strong coupling of ion fluxes (K^+ , H^+ , and Ca^{2+}) at the plasma and vacuolar membranes during stomata movements in tobacco could be simply represented as coordinated K^+/H^+ exchanges at both membranes acting in concert despite the multiplicity of ion fluxes operating in guard cells (21). The net electrogenic K^+/H^+ exchange created transient deviations of membrane voltage that, in turn, induced Ca^{2+} signals (21). Moreover, an optogenetics approach with a fungal light-gated H^+ channel demonstrated H^+ -induced cytosolic Ca^{2+} -release signals operating in Arabidopsis guard cells (22). These findings evidence the interdependence between H^+ and Ca^{2+} signaling in plant cells and position H^+ shifts as key signaling events.

Here, we show that CML18 interacts with all vacuolar NHX isoforms of Arabidopsis, NHX1 to NHX4, and have examined

¹Instituto de Química Física Blas Cabrera, Consejo Superior de Investigaciones Científicas, Madrid 28006, Spain. ²Institute of Plant Biochemistry and Photosynthesis, Consejo Superior de Investigaciones Científicas and University of Seville, Seville 41092, Spain. ³Centre for Organismal Studies, University of Heidelberg, Heidelberg 69120, Germany. ⁴Instituto de Recursos Naturales y Agrobiología, Consejo Superior de Investigaciones Científicas, Seville 41012, Spain.

*Corresponding author. Email: xalbert@iqf.csic.es (A.A.); jose.pardo@csic.es (J.M.P.)

†These authors contributed equally to this work.

the structural determinants for CML18 interaction. We found that CML18 binding is pH-dependent and essential for NHX activity. Moreover, we have determined the crystal structure of CML18 and found that this Ca^{2+} -binding protein has the exceptional feature of being intrinsically responsive to pH. Last, we have measured the dynamic changes of cytosolic pH in Arabidopsis roots in response to K^{+} availability. Limiting K^{+} triggers cytoplasmic acidification, whereas excess K^{+} produces alkalization. We propose a model in which tonoplast-localized NHX exchangers have the ability not only to modulate vacuolar pH but also, together with CML18, to monitor and respond to cytosolic pH shifts elicited by K^{+} availability to harmonize vacuolar storage with nutrient uptake. Our results support the notion that the pH-responsive NHX-CML18 module is an essential component of the cellular pH-stat.

RESULTS

CML18 binding and NHX1 activity

AtNHX1 has a cytosolic C-terminal domain encompassing residues T435 to A538 (23, 24), which contains a CML18-binding domain (CBD) that was mapped between V498 and G518 (Fig. 1A) (15, 16). CML18 binding was confirmed by a yeast two-hybrid assay (Y2H) in which the entire C-terminal cytosolic portion of NHX1 (T435 to A538) was fused to the activation domain of galactose4 (GAL4), and then tested against the CML18 protein fused to the DNA binding domain of GAL4 (Fig. 1B). The fragment required for NHX1-CML18 interaction was further delimited to a predicted amphipathic α helix comprising residues S486 to G516. A spliced mutant protein lacking this domain (NHX1 Δ CBD) tested negative in the Y2H assay (Fig. 1C).

Interaction with CML18 was reported to inhibit $\text{K}^{+}/\text{H}^{+}$ transport by NHX1 (15), but whether the CBD is essential for the transporter has not been examined. The *Saccharomyces cerevisiae* strain AXT3K carrying a deletion of the single-copy gene *ScNHX1* renders the yeast sensitive to the cationic drug hygromycin B (HygB) (25). Expression of the two major vacuolar isoforms in Arabidopsis NHX1 and NHX2 (5) suppressed the HygB sensitivity of AXT3K cells (Fig. 1C). However, selective removal of the CBD inactivated NHX1 (Fig. 1C). Preservation of the CBD was essential for the activity of AtNHX1 in yeast despite the absence of CML18 in this organism. The spurious activation of NHX1 by the resident CMD1, the only calmodulin protein produced in *S. cerevisiae*, was ruled out because Y2H assays yielded negative results (fig. S1A). Together, these results implied that the CBD is essential for AtNHX1 activity and provided a straightforward assay to dissect the regulation of AtNHX1 by CML18.

Sequence alignment of the endosomal NHX members of Arabidopsis, NHX1 to NHX6, showed that the CBD is highly conserved in the vacuolar proteins NHX1 to NHX4 and divergent in the endoplasmic reticulum and late-endosome proteins NHX5 and NHX6 (Fig. 1A). To determine whether CML18 interaction was specific for NHX1 or could be extended to other vacuolar isoforms, C-terminal fragments of NHX2 (residues G434 to P546), NHX3 (residues T438 to P552), and NHX4 (residues T437 to C529) were fused to the activation domain of GAL4 and tested against the CML18 protein fused to the DNA binding domain of GAL4. The Y2H test showed that CML18 was able to interact strongly with NHX1, NHX2, and NHX4, and more weakly with NHX3 (Fig. 2, A and B).

Protein interactions were confirmed in planta by bimolecular fluorescence complementation (BiFC) assays in *Nicotiana benthamiana*. For this assay, the full-length proteins NHX1 and NHX2 were C-terminally fused to the N-terminal half of the yellow fluorescent protein fluorophore (nYFP), and CML18 was C-terminally tagged with the C-terminal half of the YFP fluorophore (cYFP). The BiFC results confirmed that both NHX1 and NHX2 interacted with CML18 in leaves of *N. benthamiana* (Fig. 2C), whereas the NHX1 Δ CBD protein lacking the CBD lost the interaction with CML18 (Fig. 2D). Note that the NHX1-nYFP protein interacted with NHX2-cYFP in the BiFC assay (Fig. 2C), suggesting the formation of NHX1-NHX2 heterodimers in planta. BiFC fluorescence reporting the interaction of the truncated NHX1 Δ CBD protein with NHX2 was similar to that observed with wild-type (WT) proteins NHX1 and NHX2 (Fig. 2D) and labeled the tonoplast membrane, demonstrating that the NHX1 Δ CBD mutant protein was correctly sorted to the tonoplast.

Structural determinants of NHX1 for CML18 interaction

To investigate the molecular basis of the CBD-dependent activity of NHX1, we built the dimeric structure of the antiporter using the algorithms provided by the AlphaFold server (Fig. 3A) (26). The predicted structure of each protomer consists of an N-terminal pore domain formed by 13 transmembrane helices and a C-terminal cytoplasmic tail. The two protomers associate in a tail-to-tail arrangement through the interaction of their C termini. This topology was supported by the positive results of the Y2H test showing homodimerization of the C terminus of NHX1 and heterodimerization with the corresponding fragment of NHX2 (fig. S2). In each protomer, the CBD folds as a single amphipathic α helix that packs against the submembranous side of the cytoplasmic moiety of the pore domain (Fig. 3A). Furthermore, the structure suggests the physical proximity of the CBD with the hydrophobic surface comprising transmembranes TM7 and TM9 (Fig. 3B). This prediction was confirmed by a split-ubiquitin assay in yeast reporting the interaction between the pore domain (TM1 to TM9) and CBD (fig. S3). Moreover, the specific interaction of TM9 with the CBD (Fig. 3C) was substantiated through the in vivo reconstitution of the nanoluciferase (nLuc) reporter protein. Coexpression of TM9 (residues M263 to T292) fused to the large N-terminal moiety of nLuc (nLN) together with the CBD (S486 to G516) fused to the C-terminal part of nLuc (nLC) produced luminescence, whereas a control construct with the intervening stretch separating the CBD and TM13 at the pore domain (L453 to N480) fused to nLN tested negative with CBD:nLC (Fig. 3D).

Amino acids H285 and Y286 in the tail of TM9 are predicted to face residues W502 and D506 (Fig. 3C), which are themselves fully conserved in the CBD of vacuolar isoforms NHX1 to NHX4 (Fig. 1A). Mutations H285L and Y286A in TM9, as well as W502A and D506A in the CBD, all produced inactive proteins in the HygB resistance test (Fig. 3E). Because none of these peripheral residues are predicted to have a catalytic role (24), these results suggested that the physical interaction of TM9 and CBD was needed to keep NHX1 active, i.e., the CBD cis activate NHX1. Next, we tested the requirement of conserved residues H499, W502, and D506 for the interaction of the CBD of NHX1 with CML18 using Y2H assays. Results showed that W502 and D506 were essential for the interaction between the CBD and CML18 (Fig. 3F).

In the CBD, conserved amino acids H499 and D506 could form salt bridges and generate a putative pH-sensing motif. Histidine

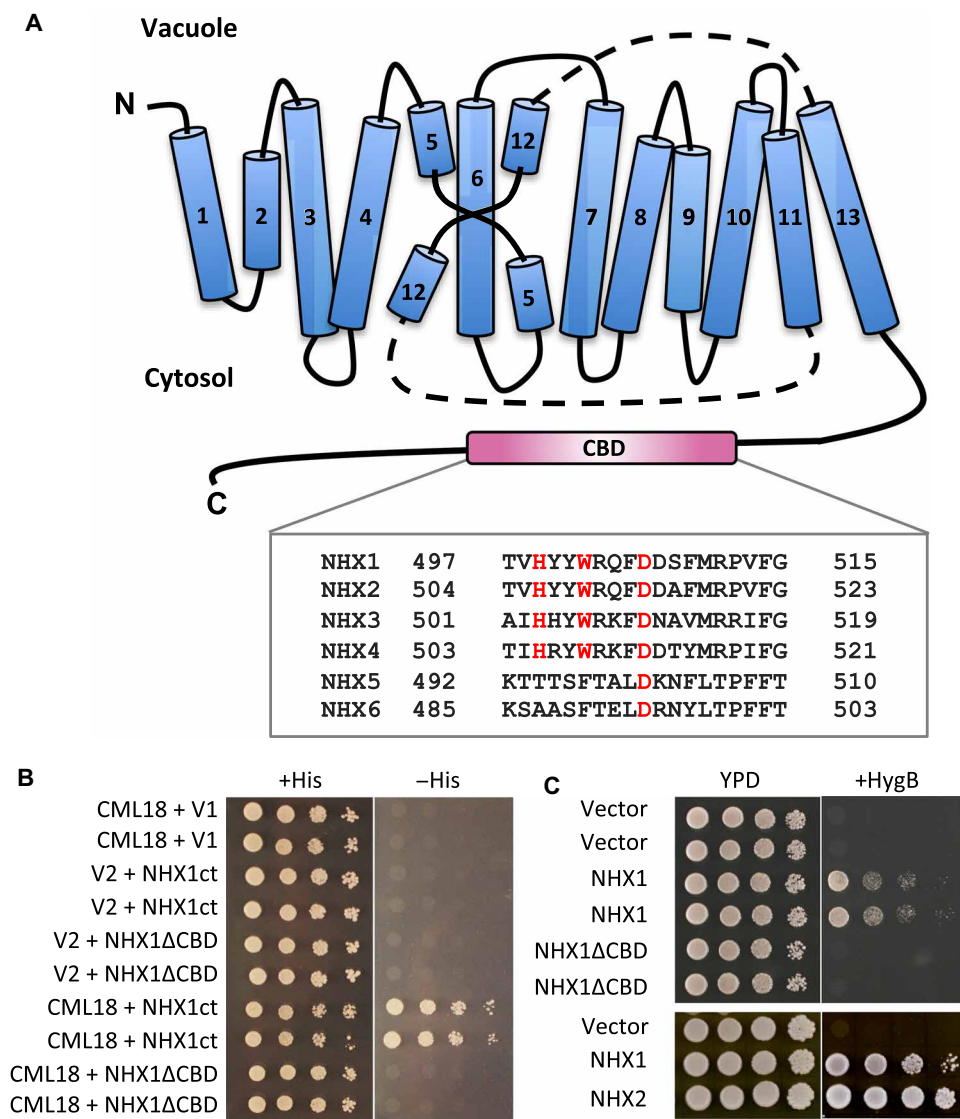


Fig. 1. The CML18-binding domain is essential for the activity of NHX1. (A) Top: Schematic representation of NHX1 topology. Blue barrels represent transmembrane (TM) segments. The semi-helices TM5 and TM12 crossed over TM6 constitute the catalytic core known as NhaA-fold. Dashed lines represent the protein loops connecting TM11, TM12, and TM13, not drawn to scale. The CBD is in the cytosolic C-terminal portion of NHX1. Bottom: Alignment of the putative CBDs of the endosomal NHX proteins of *A. thaliana* (NHX1 to NHX6). The conserved His, Trp, and Asp residues analyzed in this work are highlighted in red. (B) Yeast two-hybrid assay. NHX1 with the CBD deleted (NHX1ΔCBD, residues S486 to G516) was fused to the GAL4 binding domain in plasmid vector pGBKT7 (V1). CML18 was fused to the GAL4 activation domain in vector pGADT7 (V2). Plasmid-encoding pSV40 and p53 were used as positive controls, whereas empty vectors (V1 + V2) served as negative controls. Five-microliter drops of 10-fold serial dilutions of cells transformed with the indicated plasmids were spotted on selective YNB media without His for selection of interaction. Plates were photographed after 2 days at 28°C. Two independent transformed clones are shown for each construct. (C) Complementation assay. The cDNAs of wild-type (WT) *NHX1* and *NHX2* and mutant *NHX1ΔCBD* lacking the CBD (residues from S486 to G516) were cloned into the yeast expression vector pDRI95 and transformed into the AXT3K strain (*Δena1-4 Δnha1 Δnhx1*). Samples were processed as in (B) and plated onto yeast extract, peptone, and dextrose (YPD) plates with and without hygromycin B (+HygB; 50 μg/ml). Two independent transformed clones are shown for each plasmid in the top panel.

residues are integral to many pH sensors in proteins (27, 28), and salt bridges between histidine and acidic amino acids constitute a common pH-sensing module in proteins (29–32). Mutant proteins in residue H499 within the CBD, or in the nearby residue H479 outside the CBD as control, were expressed in AXT3K cells. Single mutants H479L and H499L, as well as the double mutant H479L-H499L, supported grow in yeast extract, peptone, and dextrose (YPD) media with HygB (Fig. 4A). However, growth assays in media buffered at

acidic or neutral pH (*S. cerevisiae* does not grow at alkaline pH) showed that proteins H499L and H499L-H479L could only support growth at pH 5 and 6 at a reduced rate relative to the WT and H479L proteins (fig. S4). The acidic to amide mutation D506N, which mimics a protonated aspartate residue, rendered the NHX1 protein inactive both alone and in combination with H499L (Fig. 4A), irrespective of the pH of the growth media (fig. S4). Furthermore, we have shown that AtNHX1 represents an H⁺ shunt that prevents excessive

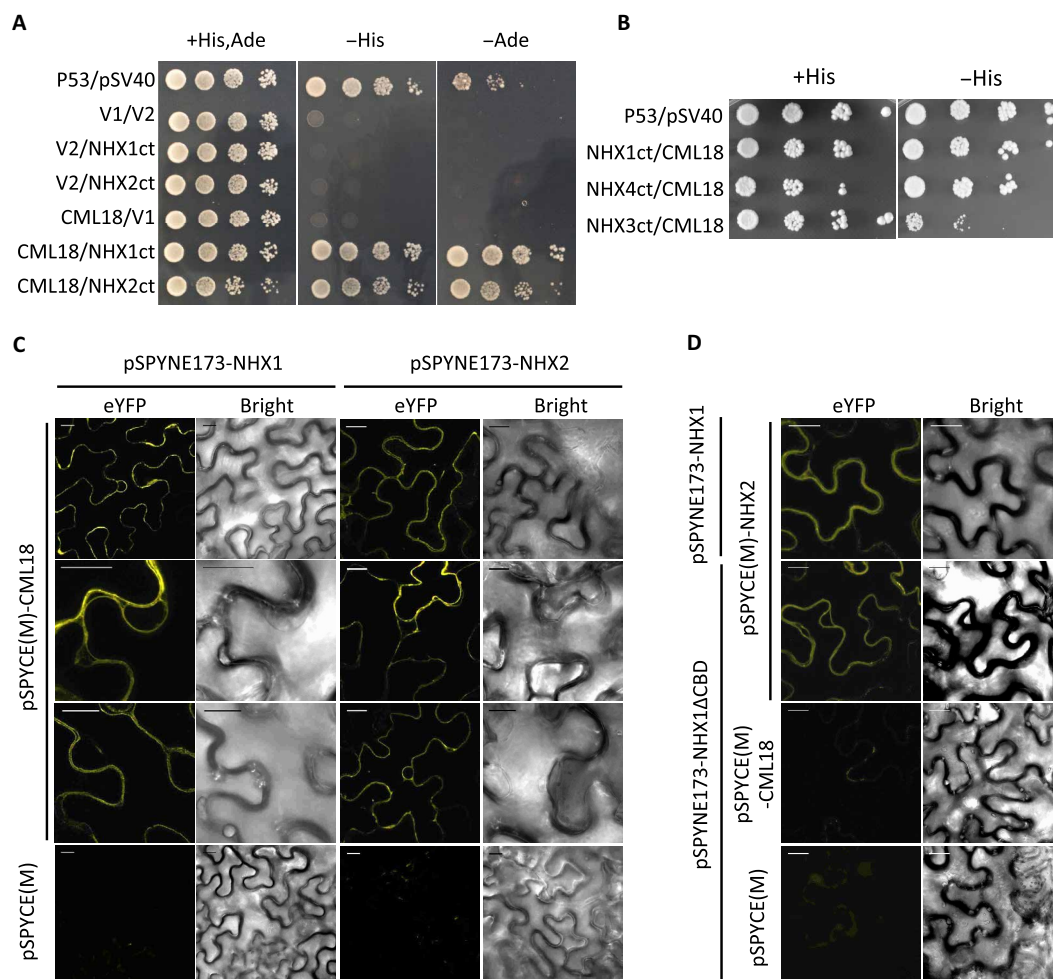


Fig. 2. CML18 binding to NHX vacuolar proteins. (A and B) Yeast two-hybrid assays. The entire C-terminal cytosolic portion of NHX1 (residues T435 to A538), NHX2 (residues G434 to P546), NHX3 (residues T438 to P552), and NHX4 (residues T437 to C529) was fused to the GAL4 binding domain in plasmid vector pGBKT7 (V1). CML18 was fused to the GAL4 activation domain in vector pGADT7 (V2). Plasmid-encoding pSV40 and p53 were used as positive controls, whereas empty vectors (V1 + V2) served as negative controls. Five-microliter drops of 10-fold serial dilutions of cells transformed with the indicated plasmids were spotted on selective YNB media without His or Ade for selection of interaction. Plates were photographed after 2 days at 28°C. (C) Bimolecular fluorescence complementation assay. Fluorescence and bright-field confocal images of *N. benthamiana* leaf sections expressing NHX1 or NHX2 fused to the N-terminal fragment of the eYFP in pSPYNE173, in combination with CML18 fused to the C-terminal fragment of the eYFP protein in pSPYCE(M). An empty vector expressing the C-terminal fragment of the eYFP was used as a negative control. (D) Interaction between NHX1 and CML18 takes place through the CBD. Confocal images of *N. benthamiana* leaf sections expressing NHX1 or NHX1ΔCBD fused to the N-terminal fragment of the eYFP in combination with NHX2 or CML18 fused to the C-terminal fragment of the eYFP protein. An empty vector pSPYCE(M) was used as a negative control. Scale bars, 20 μm.

acidification of the vacuolar lumen in the yeast mutant *nhx1* (24) and Arabidopsis stomata (18). Loading yeast vacuoles with the ratio-metric fluorescein-based pH-sensitive dye BCECF-AM (2',7'-Bis-(2-Carboxyethyl)-5-(and-6)-Carboxyfluorescein, Acetoxymethyl Ester) showed that vacuoles of yeasts expressing null mutant alleles (ΔCBD and D506N) of AtNHX1 were overly acidic, with pH_{vac} values similar to that of cells lacking the endogenous ScNhx1 protein (Fig. 4B). By contrast, vacuoles with proteins bearing mutations H479L, H499L, and H479L-H499L showed no substantial differences of pH_{vac} with the WT NHX1 control. Together, these results demonstrate that the negative charge of D506 was strictly required for NHX1 activity, whereas H499 could modulate NHX1 activity under acidic conditions that disturbed the cytosolic pH.

Although H499 was not strictly required for CML18 binding, the interaction of the NHX1-H499L protein was not as strong as with the WT NHX1. Cells coexpressing CML18 and the mutant protein H499L were able to grow in Yeast Nitrogen Base (YNB) medium minus histidine (YNB-His) but not in the more stringent media YNB-His-Ade (Fig. 4C) or when the YNB-His medium was supplemented with the HIS3 protein inhibitor 3-amino-1,2,4-triazole (Fig. 4D). Together, these results demonstrate that the acidic residue D506 and the hydrophobic W502 are essential features for CML18 binding and for protein activity in yeast, whereas H499 appears to have an ancillary function in these outputs. These results are also supportive of the strict correlation between the preservation of a functional CBD and the activity of NHX1.

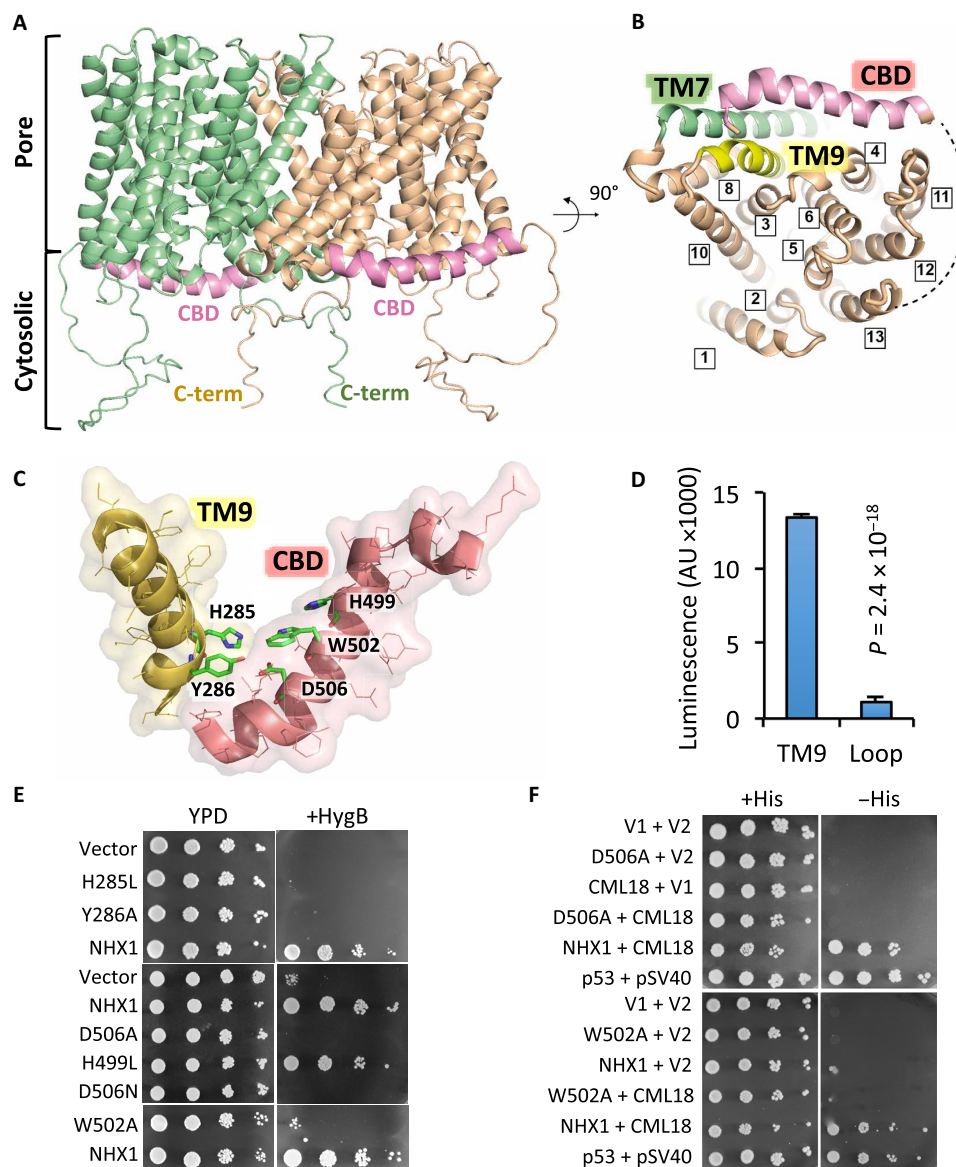


Fig. 3. Conserved residues in TM9 and CBD are essential for the activity of NHX1 and the interaction with CML18. (A) Side view of the structure of the NHX1 homodimer as predicted by the AlphaFold software. Protomers are in green and bronze colors. The CBD (pink) packs against the cytosolic side of the core TM domain forming the transporting pore. (B) Cytoplasmic view of an NHX1 protomer structure with the TM helices labeled; the CBD, TM7, and TM9 are highlighted; the dashed line represents the cytoplasmic loop connecting TM13 and CBD. (C) Intramolecular interactions between the CBD and TM9. α Helices are shown with their surface at 80% transparency, residues as thin lines, and relevant amino acid residues as green-colored backbone sticks. (D) Interaction between TM9 and CBD measured by reconstitution of nanoluciferase luminescence. The protein loop separating the CBD and TM13 (L453-N480) was used as a negative control. Shown are the means and SE of two independent experiments with two technical replicates each ($P = 2.4 \times 10^{-18}$ in unpaired t test). AU, arbitrary units. (E) Complementation test. AXT3K cultures expressing the WT NHX1 and the indicated single mutants were normalized to $OD_{600} = 0.5$, and aliquots (5 μ l) of serial decimal dilutions were spotted onto YPD plates with and without HygB (50 μ g/ml). Cells were grown at 30°C for 3 days. (F) Yeast two-hybrid assay. WT NHX1 and mutants W502A and D506A were cloned in pGBKT7 (V1) and tested for interaction with CML18 in vector pGADT7 (V2). Plasmids were transformed in strain AH109 and plated in selective YNB media with and without supplemental histidine. Empty vectors and p53/pSV40 were used as negative and positive controls, respectively. Plates were incubated at 30°C for 2 days.

Structure of CML18

To provide a full structural framework for NHX-CML18 interaction and to build a model for the regulation of NHX1 at an atomic level, we solved the crystal structure of CML18 in a complex with Ca^{2+} atoms at pH 5.6 (Fig. 5A and table S1). As expected for calmodulin-like proteins (33, 34), the structure of CML18 comprises two domains, termed N- and C-lobes, each formed by a pair of EF-hand motifs that bind

Ca^{2+} atoms. The structure also revealed two hydrophobic peptide-binding cavities that oppose the Ca^{2+} -binding sites of each domain, albeit the position of the N-lobe relative to the C-lobe resulted in an enlarged C-terminal cavity compared to that of the N-terminal half of the protein. This overall organization is stabilized by a network of hydrogen bonds involving the C-terminal residues D161, W164, and G165 at helix F4; S75 at helix E1; and R22 at helix F2 (Fig. 5A, inset).

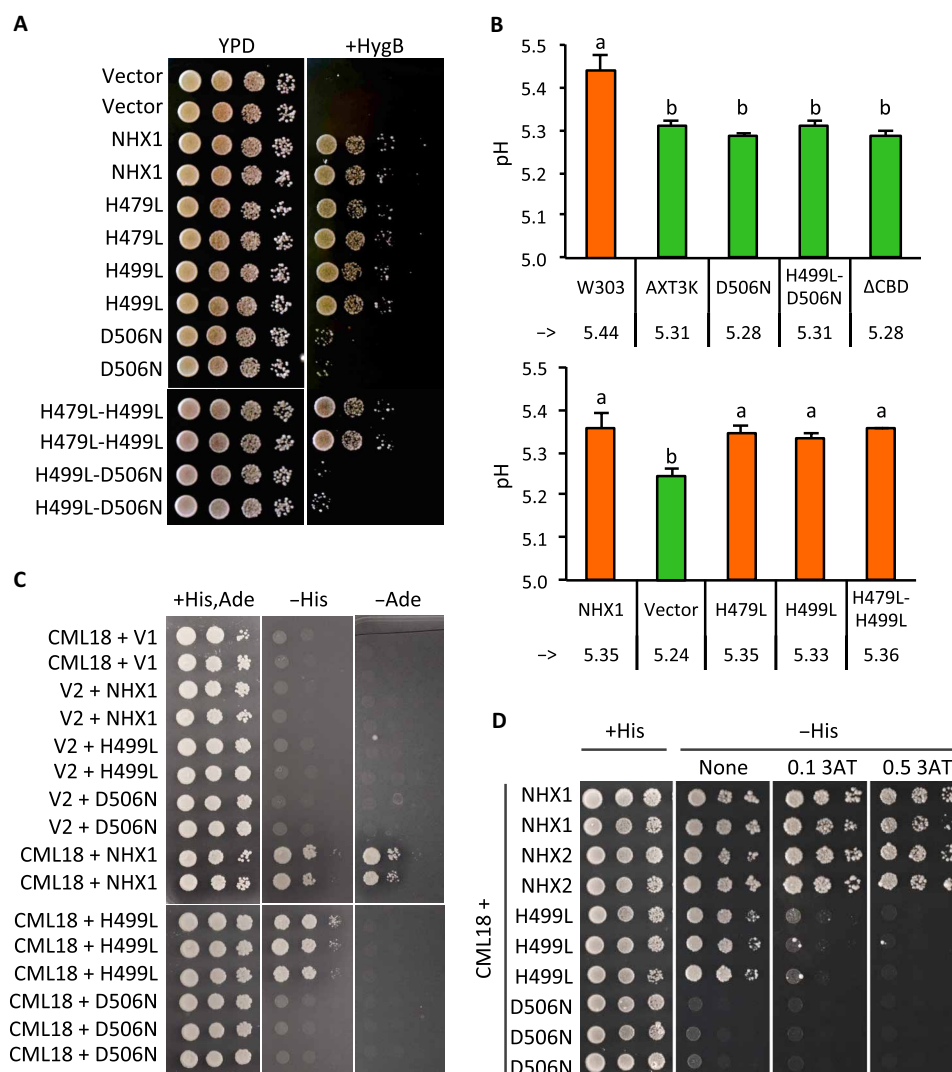


Fig. 4. Binding of CML18 is essential for AtNHX1 activity in yeast. (A) The cDNAs of *NHX1* and the mutant alleles at the indicated residues were cloned into the yeast vector pDR195 and transformed into the AXT3K strain. Overnight cultures were normalized to $OD_{600} = 0.5$, and aliquots (5 μ l) of serial decimal dilutions were spotted onto YPD plates with and without HygB (50 μ g/liter). Cells were grown at 30°C for 3 days. Shown are two independent colonies for each genotype. (B) The vacuolar pH of the WT (W303), untransformed *nhx1* mutant (AXT3K), and AXT3K expressing the indicated mutant proteins was measured by BCECF-AM. Two independent colonies (biological replicates) were used to measure vacuolar pH four times each (technical replicates). The experiment was repeated twice with similar results, and one representative measurement was presented. Data were grouped according to the biological samples tested together in the same experiment. Different letters indicate statistically significant differences in pairwise comparison by Tukey's post hoc test ($n = 8$; $P < 0.01$ in the top panel, $P < 0.05$ in the bottom panel). (C) Y2H assay. Ten-fold serial dilutions of yeast AH109, transformed with WT *NHX1* and the indicated mutants in plasmid pGBKT7 (V1), and CML18 in plasmid pGADT7 (V2) were spotted on selective YNB media without histidine or adenine for selection of interaction. Plates were photographed after 4 days at 28°C. (D) Drops were spotted on selective YNB media without histidine and supplemented with 0.1 and 0.5 mM 3-amino-1,2,4-triazole (3AT). Plates were photographed after 4 days at 28°C.

Structural response of CML18 to Ca^{2+} and pH

Typically, Ca^{2+} binding to CaM proteins results in conformational changes that lead to the exposure of hydrophobic surfaces that tether aliphatic helices to regulate or stabilize targets. To quantify Ca^{2+} binding by CML18, we performed isothermal titration calorimetry (ITC) at basic (8.3) and acidic (6.3) pH to mimic the range of physiological conditions for stressed plant cells (35). The ITC data fitted a model in which CML18 defines two sets of twin binding sites with different Ca^{2+} -binding affinities in the micromolar range (K_{d1} of $0.159 \pm 18.2 \times 10^{-3}$ and $0.106 \pm 5.24 \times 10^{-3}$ μ M; K_{d2} of $2.62 \pm 70.1 \times 10^{-3}$ and $2.42 \pm 26.3 \times 10^{-3}$ μ M, for pH 6.3 and 8.3, respectively)

(fig. S5 and table S2). These K_d values indicate distinct structural and sensing roles for each set of sites. This hypothesis is further supported by the negative ΔH observed for high-affinity (N1) sites, which is often associated with structural stabilization; in contrast, low-affinity (N2) sites tend to show positive ΔH values (34). Similar results were obtained at pH 6.3 and 8.3, showing that CML18 displays high- and low-affinity Ca^{2+} sensing properties at both pHs.

The helical content of CaMs and CMLs in solution can vary widely depending on the environmental pH (36) or upon binding Ca^{2+} (37). Hence, we investigated whether CML18 underwent conformational changes with Ca^{2+} and/or pH that could enable a differential

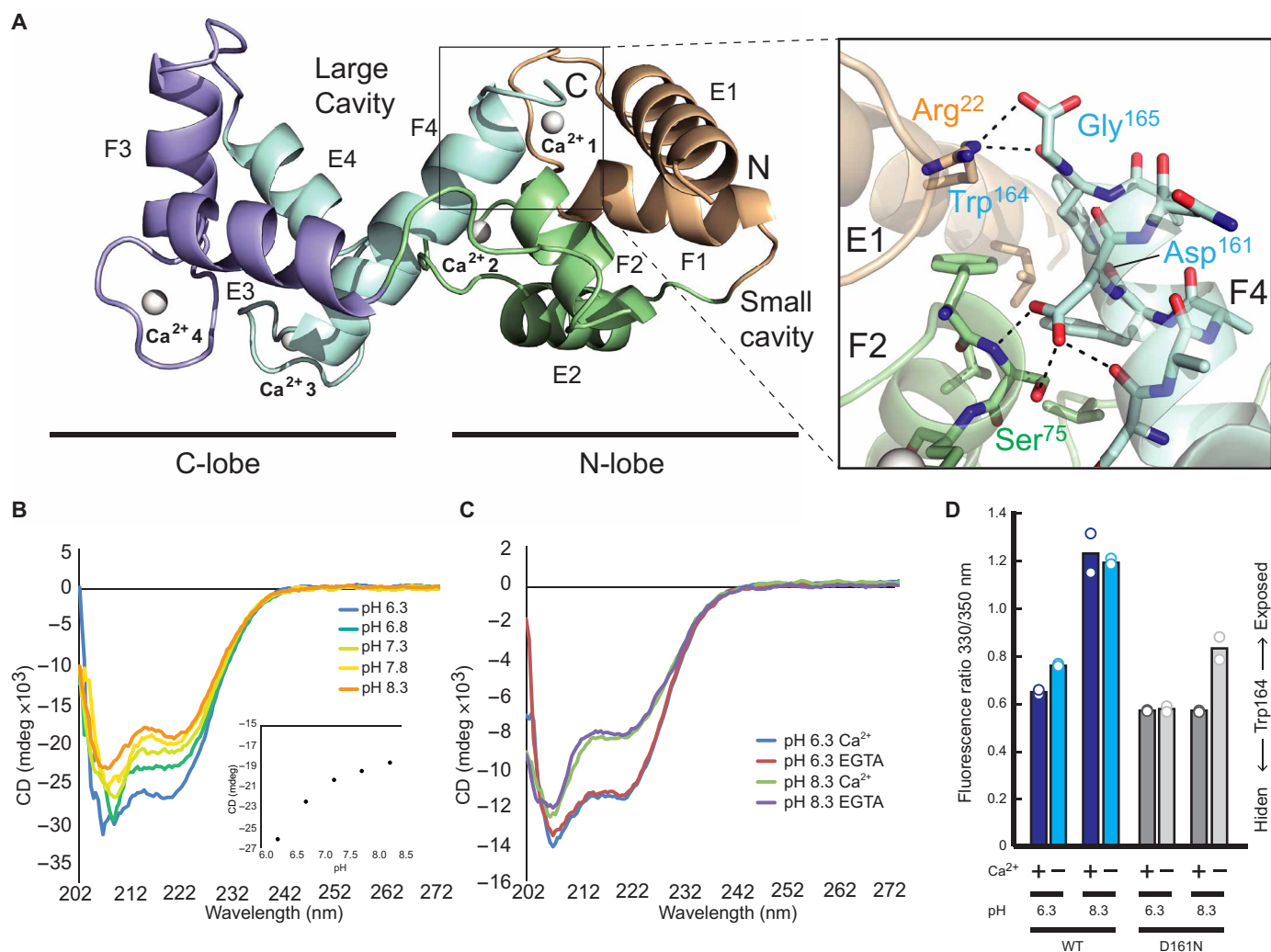


Fig. 5. CML18 conformation is sensitive to pH. (A) A cartoon representation of the crystal structure of CML18 in a complex with Ca²⁺ atoms at pH 5.6. The structure of CML18 comprises two domains, each formed by a pair of EF-hand motifs that bind two Ca²⁺ atoms. The folding produces two hydrophobic cavities that oppose the Ca²⁺-binding sites at each domain. The zoom represents a detailed view of the interactions at the N- and C-lobes interface. Notably, interactions involving residues D161 and W164 and the C-terminal carboxylate group of G165 at F4 and S75 at helix F2 stabilize the C-terminal domain in the interface between the two lobes. (B) Far-ultraviolet (UV) circular dichroism (CD) spectra of CML18 dialyzed against pHs ranging from 6.3 to 8.3. The inset represents the CD signal at 222 nm versus pH. (C) Far-UV CD spectra of CML18 at pH 6.3 and 8.3 in the presence of either 180 μM Ca²⁺ or 18 μM EGTA. (D) The ratio of the fluorescence signal at 350/330 nm (Trp¹⁶⁴ exposure) of CML18 and D161N mutant at both pH 6.3 and 8.3 in the presence or absence of Ca²⁺. D161N mutation mimics a perma-exposed Trp¹⁶⁴.

interaction with NHX1. We first analyzed the secondary structure content of CML18 by circular dichroism (CD) in the far-ultraviolet (UV) region at pH ranging from 6.3 to 8.3 (Fig. 5B). The CD spectra displayed two peaks at 222 and 208 nm, corroborating the high α -helical content found in the crystal structure. However, we observed a clear increase of the peak at 222 nm at pH 6.3 compared to pH 8.3, indicating that CML18 undergoes a conformational change that leads to higher α -helical content under acidic conditions. Conversely, no noticeable changes in the spectrum were observed upon the addition of Ca²⁺ or EGTA, implying that these changes were not a result of Ca²⁺ binding to CML18 (Fig. 5C).

CaMs often transmit the signal to downstream targets through conformational changes that involve shifting the relative position of the N- and C-lobes (34). Residue W164, which is the only tryptophan present in the protein, is ideally positioned at the interface between the

N- and C-lobes (Fig. 5A). Hence, W164 fluorescence was used as an indicator of the overall disposition of these two domains. Exciting buried tryptophan residues at 285 nm results in fluorescence emission at 330 nm; a red shift in emission wavelengths toward ≈ 354 nm is widely considered indicative of decreased hydrophobicity around the emitting tryptophan residues (38). Thus, a change in the ratio between the fluorescence emission at 350 and 330 nm would report on conformational changes in the W164 environment and, consequently, on the structural layout of the protein. Data showed a remarkable red shift effect when comparing CML18 fluorescence at pH 6.3 and 8.3 (Fig. 5D), indicating that the crystal structure obtained likely corresponds to the 6.3 conformation (crystal obtained at pH 5.6) and that a pH increase triggers a conformational rearrangement between the N- and C-lobes. These data also imply that residue W164 is buried in the interface region between the N- and C-lobes at acidic pH and exposed at alkaline pH.

No histidine side chain might act as a pH-sensitive relay at the interface between the N- and C-terminal domains of CML18. However, the CML18 structure revealed that residue D161 is buried into the interface between lobes making polar contacts while surrounded by nonpolar residues despite its carboxylate side chain (Fig. 5A). D161 is the unique charged amino acid stabilizing the relative conformation of the N-terminal and the C-terminal lobes. Since the burial of acidic residues is usually coupled with an increase in their pK_a (where K_a is the acid dissociation constant) (39), we hypothesized that the reversible protonation of the buried D161 carboxylate side chain could be involved in the conformational changes observed in the structural transition from pH 6.3 to pH 8.3. To corroborate this hypothesis, we purified a mutated version of CML18 in which D161 was replaced by asparagine (D161N) to mimic an aspartate residue in a permanently protonated state. Fluorescence experiments with the CML18-D161N mutant confirmed that the ratio of 350-nm/330-nm emissions matched that of WT CML18 protonated state at pH 6.3 and remained constant regardless of pH (Fig. 5D). Moreover, the far-UV CD spectra of CML18-D161N was nearly identical to that of the WT protein at pH 6.3 corroborating that the mutant protein displayed the same conformation as the WT protein at pH 6.3 (fig. S6). In summary, our data support residue D161 acting as a key feature for sensing pH, potentially regulating the conformational flexibility that controls NHX1 binding.

Together, the CD and fluorescence data strongly indicate that, besides being a Ca^{2+} -binding protein, CML18 has a pH-sensing ability that leads to a conformational change involving the interface between N- and C-terminal domains. An increase in pH leads to D161 deprotonation, the exposure of W164, and a concomitant reduction of protein helicity. In this regard, it is important to note that the alignment of CML18 with the rest of the 55 CMLs from *Arabidopsis* (40) showed that the C-terminal sequence “DxxWG” harboring D161 and W164 is solely shared with CML17 (fig. S7), suggesting a unique pH-sensing structural feature among CML proteins.

pH-dependent interaction of CML18 with NHX1

Our data suggest that local pH variations and Ca^{2+} concentration dictate the conformational state of CML18 which is compatible with NHX1 recognition. Hence, we analyzed the pH and Ca^{2+} dependence of CML18 interaction with a synthetic peptide corresponding to the CML18-binding motif of NHX1 (CML-BD peptide, residues D485 to R518) using CD spectroscopy. Data showed that whereas

CML-BD in solution has no helical content, the mixture CML-BD with CML18 at pH 6.3 displayed an increased α -helical content relative to that of CML18 alone (Fig. 6). This increased helicity may be attributable to the folding of CML-BD into the binding pocket of CML18 since the spectrum of the mixture was more negative than the sum of each individual spectrum of CML-BD and CML18 taken separately. However, only a small increase in helicity was observed in the spectra when the mixture was prepared at pH 8.3 (Fig. 6), suggesting the idea that the binding of CML18 to CML-BD is mostly favored at acidic pH.

ITC experiments carried out at pH 6.3 with or without Ca^{2+} using WT CML18 supported these results (fig. S5, C and D). The K_d value of CML18 for CML-BD was 3.02 μ M in the presence of 180 μ M Ca^{2+} and 2.21 μ M in the presence of 18 μ M EGTA (table S3). Our data fit a model with two CML-BD binding sites with equal affinity per CML18 monomer, suggesting the idea that two CML-BD peptides can interact with CML18 through both of its binding cavities. Ca^{2+} seems to reinforce the interaction as the occupancy of these sites is reduced upon EGTA addition. In summary, our data indicate that variations in pH lead to conformational changes that affect the binding of CML18 to CML-BD. Specifically, our findings show that a high-affinity complex is formed at pH 6.3 in the presence of Ca^{2+} , while no interaction is observed at pH 8.3 in the absence of Ca^{2+} .

Structure of the CML18-CBD complex

To analyze the structural basis of the interaction of CML18 with NHX1 and to integrate biochemical and structural data, we modeled the structure of a complex of CML18 with the CBD of NHX1 using the algorithms provided by the AlphaFold server (Fig. 7) (26). The server was unable to predict the domain organization determined by the crystal structure of CML18, as frequently observed for flexible proteins that undergo conformational changes (41). Hence, to build the model, we first predicted the structure of the individual N and C domains of CML18 in complex with a copy of the CBD peptide, and then assembled them into a single model using the structure of CML18 at pH 6.3 as a template. The resulting model displayed a root mean square deviation of 0.99 Å for 162 matched C α atoms, thus indicating that our experimental crystal structure might reflect an active form of CML18 despite that no CBD peptide was included in the crystallization conditions. We focused our analysis on the interaction of CBD and the large cavity of CML18 formed in the interface between domains because the pH-dependent structural reorganization

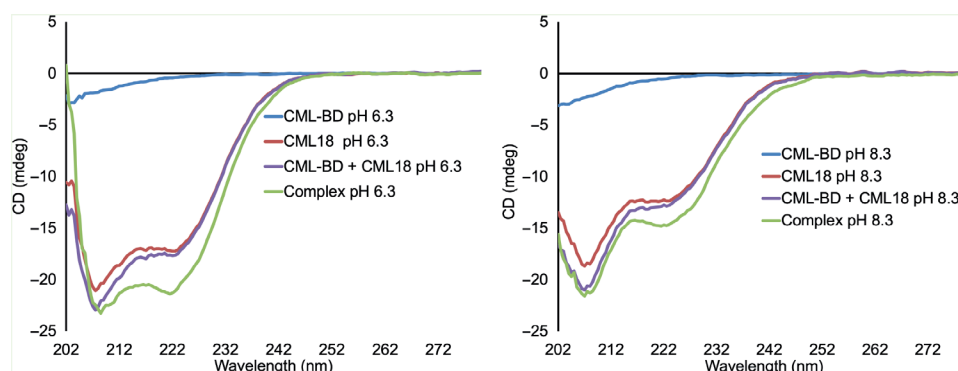


Fig. 6. pH-dependent interaction between CBD peptide and CML18. Far-UV CD spectra of CML18, CBD peptide, and a mixture of them at both pH 6.3 (left) and 8.3 (right). The expected spectrum for noninteracting samples, calculated as the sum of both spectra, is represented in purple.

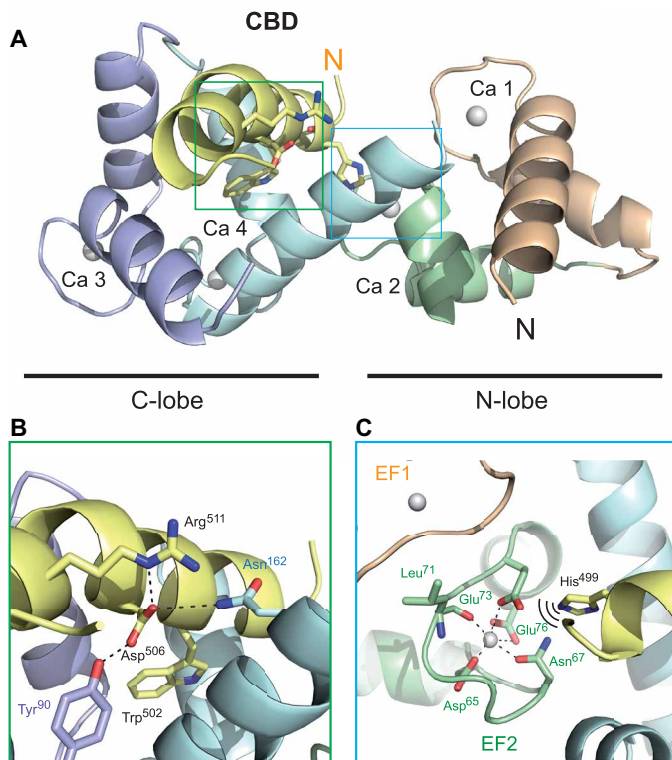


Fig. 7. Model showing the interaction of the CBD peptide with CML18. (A) Structural model of the CBD peptide (in pale yellow) bound to the large cavity of CML18. (B and C) Detailed view of the interaction between the CBD peptide and CML18 showing the interaction pattern of D506 (B) and H499 with EF2 (C).

of CML18 occurred at this cavity (Fig. 5A). As suggested by the analysis of the CD spectra of the complex between CML18 and CML-BD (Fig. 6), our model shows that the CBD folds as an amphipathic helix buried into the hydrophobic cavity defined by CML18's EF hands (Fig. 7A). For this to happen in the context of the formation of a complex between CML18 and NHX1, the CBD should detach from the transmembrane domain of NHX1 as CML18 binding involves residues facing the core of the transporter (Fig. 7B). Specifically, the binding of the CBD to CML18 would imply the burial of the W502 and D506 facing TM7 to TM9 (Fig. 7C), which is coherent with these residues being required for both CML18 binding and NHX1 activity. Together, these results imply that CML18 binding should be inhibitory to NHX1 exchanger activity as it would prevent the stacking of the CBD against the pore domain.

Response of cytosolic pH to K^+ availability

The activity of the tonoplast exchangers NHX1 and NHX2 is critical for the cellular K^+ homeostasis of Arabidopsis through the active uptake of K^+ into vacuoles (5, 18). To provide a physiological context to the Ca^{2+} - and pH-dependent interaction of NHX1 with CML18, we measured the shifts in cytosolic pH in response to K^+ availability. For this, we used Arabidopsis plants expressing the genetically encoded dual sensor R-GECO1- E^2 GFP to monitor changes in Ca^{2+} and H^+ concentrations (42). The R-GECO1 moiety is an intensimetric Ca^{2+} sensor, meaning that the intensity of fluorescence emission increases with the concentration of Ca^{2+} . By contrast, E^2 GFP is a ratiometric pH sensor, which allows the measurement of cytosolic pH from the

ratio green to cyan fluorescence (R), where green is the 488-nm pH-dependent E^2 GFP signal, and cyan the 458-nm pH-independent E^2 GFP signal. Therefore, the R-GECO1- E^2 GFP line can be used to monitor changes in cytosolic pH and Ca^{2+} levels simultaneously.

R-GECO1- E^2 GFP reporting seedlings were first incubated in imaging buffer [IB; 5 mM KCl, 50 μ M $CaCl_2$, and 10 mM MES-tris (pH 5.6)] for 15 min, next transferred to IB without KCl (IB – KCl) or with KCl (IB + 50 mM KCl), and fluorescence emissions in roots for R-GECO1 and E^2 GFP channels were captured sequentially after 20 min of incubation. The region of interest (ROI) was defined as the area where the major changes in pH-derived fluorescence ratios were observed, specifically up to 455 μ m upward from the quiescent center. The results (Fig. 8) showed that K^+ deprivation elicited an acidic shift in the cytosol from $pH\ 7.39 \pm 0.1$ (means \pm SD) to $pH\ 7.22 \pm 0.1$, whereas the high- K^+ treatment had the opposite effect and produced cytoplasmic alkalization to $pH\ 7.85 \pm 0.23$ ($n = 33$ to 34 seedlings per treatment). In these conditions, no statistically significant change in cytosolic free Ca^{2+} was observed under K^+ depletion when the entire ROI was considered, whereas the transfer to high K^+ produced the apparent decline in Ca^{2+} concentration in the time frame analyzed. However, a local increase in free Ca^{2+} was noticeable at the root tip in K^+ -limiting conditions. In both control and $-K^+$ conditions, the Ca^{2+} maxima occurred in the early elongation zone of the root, which has been described as the K^+ -sensing niche (43). These Ca^{2+} maxima were quenched by the 50 mM K^+ treatment. Together, the cell biology and protein binding data suggest the preferential interaction of CML18 and NHX1 at the acidic pH of cells deprived of K^+ , a condition in which the exchange of vacuolar H^+ for cytosolic K^+ mediated by NHX1/2 should be inhibited to prevent further deviations from the homeostatic pH values.

Role of CML17 and CML18 in K^+ accumulation

The alignment of CML18 with the other 55 CaM and CML proteins encoded in the Arabidopsis genome showed that the C-terminal sequence “DxxWG” harboring key residues D161 and W164 is shared with CML17 only (fig. S7), suggesting the idea that this motif is a unique structural feature of CML17 and CML18 among CaM/CML proteins. Therefore, we next analyzed the response of *cml17* and *cml18* mutant plants to high external K^+ , a process in which NHX function in vacuoles is paramount (5). Proteins NHX1 and NHX2 are essential for the vacuolar partitioning of excess K^+ , and failure to do so results in K^+ toxicity presumably owing to the uncoupling of uptake and compartmentation (5).

Transferred DNA (T-DNA) insertion lines SALK_069855 (*cml17*) and SALK_033749 (*cml18*) were used to produce homozygous single and double *cml17 cml18* mutant lines. Gene disruption and lack of mRNA were confirmed by diagnostic polymerase chain reaction (PCR) and reverse transcription PCR (RT-PCR), respectively (fig. S8). The *cml18* mutant accumulated more K^+ in shoots compared to the WT control, but only the double mutant *cml17 cml18* was more resistant to treatment with 20 to 40 mM K^+ and grew less in 1 mM K^+ than either single mutant, suggesting functional redundancy of CML17 and CML18 in K^+ homeostasis (fig. S9). The high- K^+ tolerance of *cml17 cml18* plants correlated with enhanced accumulation of K^+ in shoots but not in roots of plants, regardless of whether the K^+ was added as sulfate or chloride salts (Fig. 9 and fig. S10). Note that the concentration of K^+ measured in the cell sap of shoots growing in high K^+ exceeded the homeostatic value of 80 to 100 mM in the cell cytosol and thus likely reflected the vacuolar accumulation of

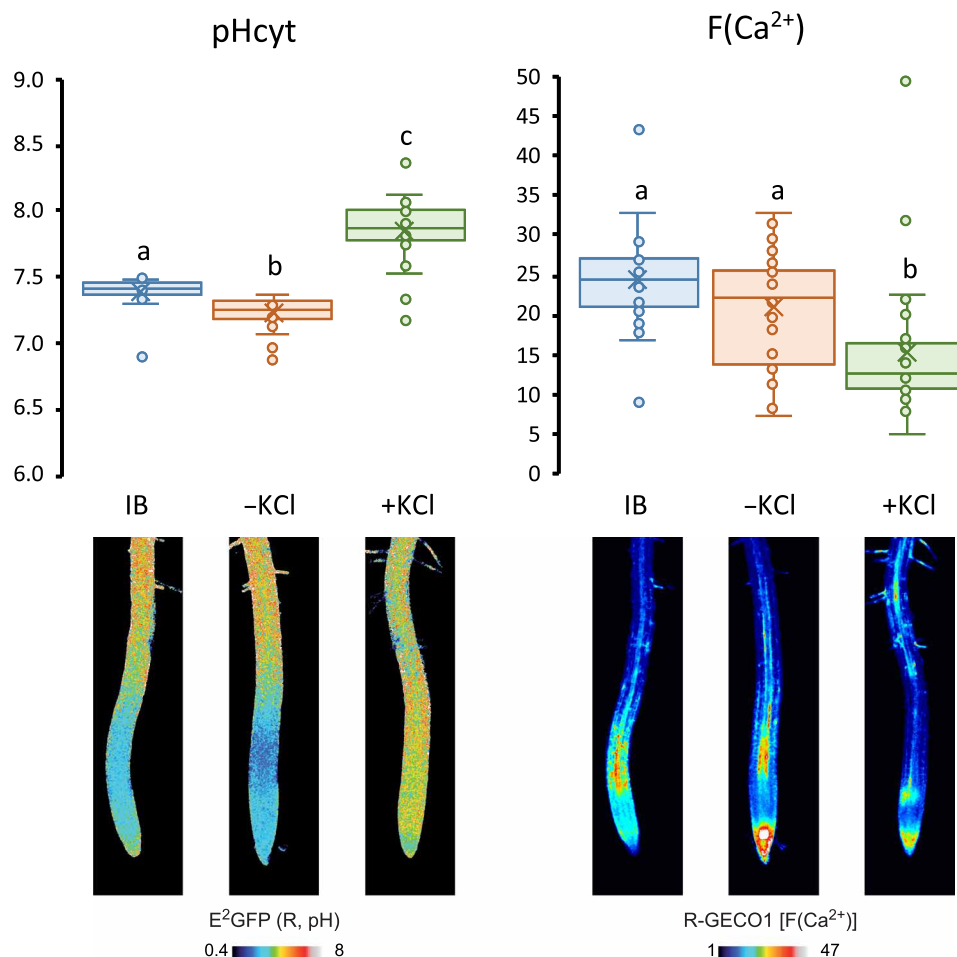


Fig. 8. Changes in cytosolic pH and free Ca²⁺ concentration elicited by differential K⁺ availability. Fluorescence emitted by roots of the R-GECO1–E²GFP line was captured 20 min after transferring the seedlings from imaging buffer (IB) with 5 mM KCl to IB without K⁺ (–KCl) or with 50 mM KCl (+KCl). Top: Ratiometric fluorescence of E²GFP was converted to pH values, whereas the intensimetric fluorescence of R-GECO1 is given as arbitrary fluorescence units [F(Ca²⁺)]. The box plots present quartiles Q1 to Q3. The X symbols are the means. Data are of 33 to 35 individual seedlings per treatment, compiled from two independent experiments. Outlier data points were not excluded from statistical analyses. Letters indicate statistical significance at $P < 0.01$ (two-tailed t test). Bottom: Representative seedlings of each treatment.

surplus K⁺, a process that is facilitated by vacuolar NHX proteins (5, 18, 44). These findings are coherent with greater activity of vacuolar NHXs in plants lacking CML18 and indicate an inhibitory role of CML17/CML18 proteins leading to the vacuolar accumulation of K⁺ in the shoot. Unexpectedly, CML17 failed to demonstrate interaction with vacuolar NHX1 to NHX4 proteins in Y2H assays (fig. S1B), implying the likely existence of additional target proteins involved in K⁺ homeostasis in Arabidopsis.

DISCUSSION

Potassium is an essential macronutrient that plants accumulate in large quantities, exceeding purely nutritional requirements. The cytosolic K⁺ content is maintained within narrow homeostatic limits of 80 to 100 mM, and the surplus K⁺ taken up by well-fed plants is stored in vacuoles (45, 46). Vacuolar K⁺ serves to replenish a declining cytosolic pool, drives rapid osmotic adjustments supporting stomatal movements, and contributes to the regulation of vacuolar pH (5, 18, 45, 47). Vacuolar NHX proteins are K⁺/H⁺ antiporters

energized by the pH gradient across the tonoplast and, hence, key players in the accumulation of K⁺ against the concentration gradient (5, 18, 44). The activity of NHX1 and NHX2 prevents poisoning by high-K⁺ supplements (5).

Vacuolar K⁺/H⁺ exchange has long been suspected to be instrumental in cytosolic pH regulation (21, 48). Here, we have shown that K⁺ deprivation leads, within minutes, to cytosolic acidification in Arabidopsis roots (Fig. 8). In these conditions, K⁺/H⁺ exchange by NHX proteins must be inhibited to halt compartmentalizing K⁺ and releasing H⁺ back to the cytosol, which would worsen the consequences of K⁺ starvation. Conversely, transfer from moderate (5 mM KCl) to high-K⁺ media (50 mM KCl) elevated the cytosolic pH, presumably through enhanced H⁺ pumping at the plasma membrane (48). Under enhanced K⁺ uptake, NHX exchangers should be active to compartmentalize excess K⁺ while releasing H⁺ from the vacuole to counteract cytosolic alkalization (5). Our biochemical data indicate that CML18 binding to NHX1 is favored by acidic conditions, and thus, we conclude that CML18 binding is likely inhibitory for K⁺/H⁺ exchange. In line with this notion, a mutant plant lacking

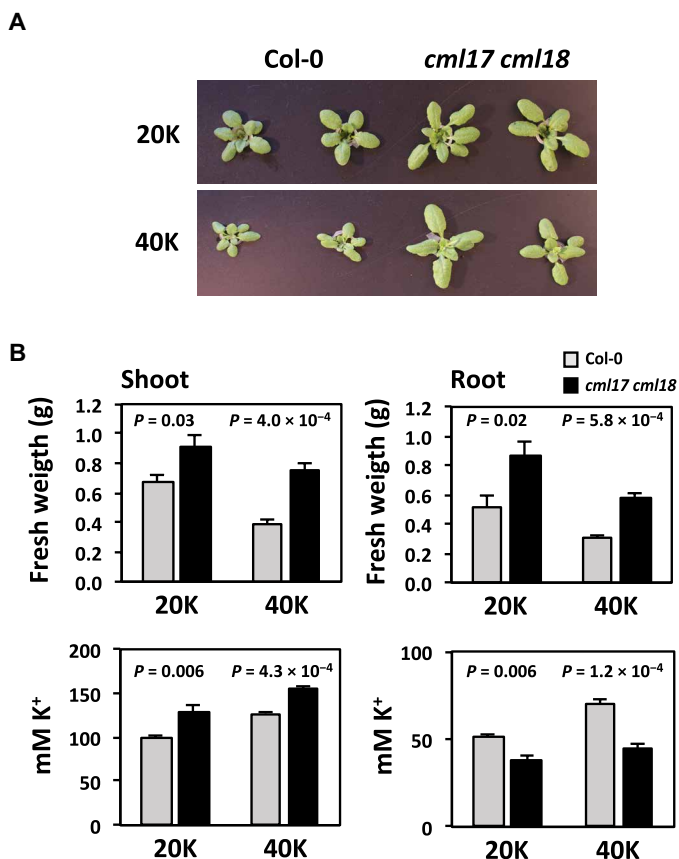


Fig. 9. Enhanced growth of *cml17 cml18* mutant plants under high potassium. Plants of genotype Col-0 and *cml17 cml18* were grown for 2 weeks in hydroponic culture with LAK medium and then transferred to fresh media with the indicated concentrations of K_2SO_4 for 2 weeks before harvesting. (A) Two representative plants of each genotype and condition at harvest. (B) Means and SE of fresh weight and K^+ concentration in the cell sap of shoots and roots. The P values for WT versus mutant comparisons are given (two-tailed t test, $n = 5$ to 6 plants per genotype and treatment).

both CML17 and CML18 showed enhanced resistance to high K^+ supply. A caveat is that a single mutant allele was available for each gene in the public repository ABRC (TAIR release 11). However, the consistent phenotype and additive effects of *cml17* and *cml18* mutations in providing resistance to high K^+ argues against an artifact produced by a hidden T-DNA insertion outside these genes.

The inhibitory effect of CML18 on NHX activity is coherent with the recent finding of enhanced salt tolerance imparted by mutant NHX1 proteins unable to interact with CML18 (16) and the previously reported inhibition of K^+/H^+ and Na^+/H^+ exchange rates of NHX1 upon CML18 binding (15). Although CML17 and CML18 appeared to have a redundant role in setting the tolerance of Arabidopsis plants to high- K^+ treatment, CML17 failed to demonstrate interaction with the C termini of vacuolar proteins NHX1 to NHX4 in a Y2H assay (fig. S1) implying that CML17 targets other K^+ transporters yet to be identified but different from the NHX1 to NHX4 proteins. Genes *NHX1*, *NHX2*, and *CML18* are widely expressed in leaves and roots of Arabidopsis, but *CML17* is expressed at very low levels in the leaf and not in roots according to RNA sequencing data in public databases. The FDNxW/F motif is conserved at the

C-terminal end of CML18 orthologs from dicots and monocots (www.orthodb.org/?gene=Q9M8U1), suggesting the idea that the pH-sensing ability is preserved across plant species.

Notwithstanding the inhibitory role of CML18, mutant variants of NHX1 unable to bind CML18 behaved as dead proteins in the yeast complementation tests. NHX1 proteins bearing deletions of the CBD, or the single point mutations W502 and D506N/A that had lost the ability to bind CML18, were also unable to suppress the sensitivity of the *nhx1* mutant to HygB. Tryptophan residues in calmodulin-binding domains are usually nudged into hydrophobic pockets of calmodulin proteins and mutation of the conserved W502 in the CBD inactivated NHX1 and impeded the interaction with CML18 (Figs. 2 and 3). These results imply that the structural integrity of the CBD is strictly required for NHX1 operation, which is counterintuitive given the inhibitory effect of CML18. According to the AlphaFold structural model, the CBD is in the vicinity of TM7 to TM9 in the pore domain, and a nanoLuc reconstitution assay confirmed the physical interaction of TM9 with CDB (Fig. 3). The structural model also revealed the interacting pair consisting of H285 and D506, which connects the two domains and appears to stabilize the helical conformation. Mutation of conserved residues H285 and Y286 at the tail of TM9, and of W502 and D506 in the CBD, all inactivated NHX1, demonstrating that these peripheral residues are essential for NHX1 activity. Together, these data suggest that the interactions of D506 with CML18 or with H285 in TM9 are mutually exclusive. Our findings strongly suggest that the interaction of the CBD with TM9 keeps NHX1 in the active form and that CML18 binding likely interrupts this interaction to inhibit NHX1 (Fig. 10). Structural studies on NHX homologs suggest a mechanism where the transition from outward- to inward-facing conformations of the antiporter facilitates the loading and delivery of substrate ions across the membrane (49–51). In this regard, the human Na^+/H^+ antiporter NHE1 displays a helix topologically equivalent to the CBD of NHX1 to NHX4 that is required for this transition, as it stabilized more extensive interactions with the transmembrane domain in one conformation compared to the other (52). The NHX1-CML18 conformations shown in Fig. 10 are inspired by the structures of the NHE1-CHP1 complex (52). The CML18-dependent displacement of the CBD from the NHX1 pore domain would likely block the antiporter in one of these conformations, impeding K^+/H^+ transport. This inhibition mechanism is likely activated by cytosolic acidification, as illustrated by the pH-responsive nature of CML18 and the greater affinity of CML18 for the NHX1-derived calmodulin-binding peptide comprising those residues forming the CBD (Fig. 6). Cytosolic acidification may result from K^+ starvation (Fig. 8), a physiological condition in which K^+/H^+ exchange at the tonoplast must be inhibited.

Despite the fact that we have corroborated that CML18 is a Ca^{2+} -binding protein at physiological concentrations (table S2), the comparative analysis of the CD and the fluorescence spectrum of CML18 in the presence or absence of Ca^{2+} did not reveal any remarkable structural differences (Fig. 5C). In contrast, the Arabidopsis CMLs characterized to date, including CML7 (53), CML19 (54), CML15, CML16 (55), and CML35 (56) all display Ca^{2+} -dependent conformational changes that lead to the binding to their respective targets. In this regard, ITC data suggest a marginal Ca^{2+} dependence of the binding of CML18 to CBD peptide, whereas the modeled structure of the complex between CBD and CML18 revealed a close contact between H499 at the CML-BD and the Ca^{2+} -binding site at EF-hand

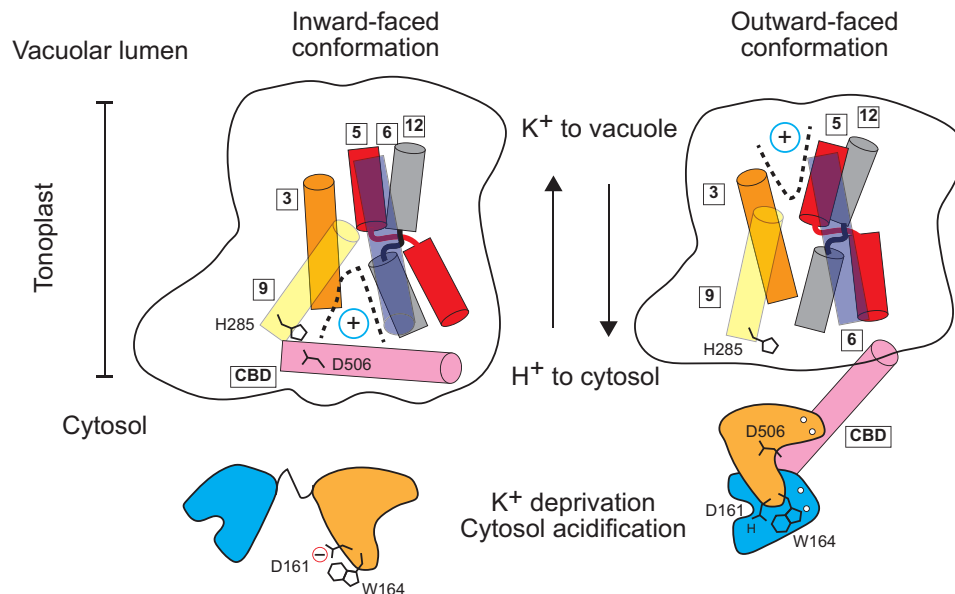


Fig. 10. Model for the regulation of vacuolar K^+/H^+ exchangers by the pH-sensitive calmodulin-like protein CML18. Working model representing the role of CML18 in the regulation of NHX1. In the NHX1 protomer, the helices forming the ion-conducting pore are shown in two conformations, inward facing and outward facing. The active center is located at the junction between TM5 and TM12, with NHX1 exchanger activity depending on the transition between these conformations. NHX1 pumps K^+ into the vacuole and H^+ into the cytoplasm. K^+ deficiency leads to cytosol acidification, which triggers a CML18 conformational change that facilitates the interaction with NHX1 via the CBD and the subsequent inhibition of K^+ transport into the vacuole. Disruption of the H285-D506 interaction in NHX1 disables ion transport. The two lobes of CML18 are depicted in blue and orange. The residues involved in the pH-responsive conformation CML18 at low pH (D161 and W164) are indicated.

2 (EF2) of CML18 (Fig. 7). This interaction could explain the variable affinity of CML18 for CBD under different Ca^{2+} and pH conditions and the diminished interaction of the NHX1 mutant H499L and CML18 (Fig. 4). We envision that, at acidic pH, H499 is positively charged and interacts with the negatively charged carboxyl group of EF2. Our findings show that at higher pH levels and lower Ca^{2+} concentrations, the interaction between CML18 and CBD is hindered (Fig. 6). Deprotonation of H499, together with the associated conformational changes in CML18 structure, would facilitate the release of CBD from CML18, in turn restoring the active conformation of NHX1 through the re-establishment of the H285-D506 pair (Fig. 4).

By determining the crystal structure of CML18 under acidic pH conditions, we have established a framework that has allowed us to study whether Ca^{2+} concentration or pH governs its interaction with NHX1. CML18 consists of two domains, each containing two Ca^{2+} -binding EF-hand motifs. Each pair defines a hydrophilic cavity that might be suitable for binding to the CBD (Fig. 7). The joined analysis of CD and fluorescence spectra of CML18 uncovered a pH-dependent structural rearrangement involving the relative position of the N- and C-lobes (Fig. 5). The analysis of the crystal structure suggested that the protonation/deprotonation of the terminal residue D161 could be responsible for this transition. Supporting this, the CML18-D161N mutant, which mimics a permanently protonated version of this residue, adopts the conformation of CML18 at low pH. We additionally showed that the binding of CML18 to a synthetic peptide comprising the CBD was largely enhanced at acidic pH (Fig. 6). Thus, our data suggest that CML18 constitutes a molecular pH sensor. Most of the structural changes triggered by pH occur within the pH range observed in cells deprived/supplemented with K^+ (Fig. 8).

In a wider perspective, the activity of tonoplast-localized NHX exchangers must be finely tuned with that of vacuolar K^+ channels mediating intracellular K^+ distribution to preserve homeostatic K^+ concentrations in the cytosol (46, 57). Vacuolar TPK channels are highly selective for K^+ ions, mechanoresponsive to turgor, insensitive to tonoplast voltages, and activated by cytosolic calcium through their C-terminal EF hands (58). TPK1, the most abundant TPK/KCO isoform in Arabidopsis, has been involved in vacuolar K^+ release (59). TPK1 is regulated by pHcyt, showing a maximal open probability at acidic that declined rapidly as the pH became more alkaline (59). Together, these data suggest that TPK1 might release vacuolar K^+ when the cytosolic K^+ pool declines, the cytosol becomes acidic, and vacuolar NHX exchangers are inhibited by CML18 binding. Conversely, TPK1 closes upon the alkaline shift promoted by excess K^+ and Na^+ , conditions in which NHX1/2 are actively compartmentalizing these ions. Our findings define an integrative model in which K^+ -selective transporters at the tonoplast respond to physiological changes in pHcyt elicited by K^+ availability and provide a molecular mechanism supporting the long-standing notion that vacuolar K^+ not only acts as a reservoir to buffer fluctuations in the cytoplasmic K^+ concentration. Our data highlight the contribution of vacuolar K^+ fluxes to the cellular pH-stat and the reciprocal regulation of cytosolic pH and the vacuolar K^+ store. Moreover, we have identified the atypical calmodulin-like protein CML18 as a pH-sensing protein controlling the activity of the major K^+/H^+ exchangers at the tonoplast.

MATERIALS AND METHODS

Expression and purification of CML18 in *E. coli*

The CML18 cDNA from *A. thaliana* was cloned into a pETDuet expression plasmid to yield pETDuet-His-CML18. The plasmid

was transformed into *Escherichia coli* strain BL21(DE3) for protein expression. Ten-milliliter aliquots of an overnight starter culture were subcultured into 700 ml of fresh 2TY culture broth (8 g of tryptone, 5 g of yeast extract, 2.5 g of NaCl per liter of solution) plus ampicillin (50 µg/ml) and allowed to grow to $DO_{600} = 0.7$. Protein expression was induced overnight with 0.3 mM isopropyl- β -D-thiogalactopyranoside. Cells were harvested by centrifugation. The cell pellet was resuspended in buffer A [50 mM tris (pH 7.5), 150 mM NaCl, 5 mM $CaCl_2$, 10 mM imidazole, and 2 mM dithiothreitol (DTT)]. Cells were lysed by sonication and centrifuged (45 min, 16,000 rpm, 277 K, SS-34 rotor). The clear supernatant was then filtered through a 0.45-µm pore diameter filter (Millipore) and loaded into a 1-ml Ni Sepharose column (GE Healthcare) previously equilibrated with buffer A. A washing step with five column volumes of buffer A followed by five volumes of buffer containing 50 mM tris (pH 7.5), 150 mM NaCl, 5 mM $CaCl_2$, 40 mM imidazole, and 2 mM DTT was performed. The column was then re-equilibrated with buffer A, and thrombin protease (Merck) was loaded for overnight digestion at 293 K. Cleaved CML18 was eluted with buffer A. The sample buffer was changed to buffer B [50 mM tris (pH 7.5), 150 mM NaCl, 5 mM $CaCl_2$, and 2 mM DTT] using a PD-10 desalting column (Cytiva). To remove trace contaminants, the sample was then loaded into a gel filtration Superdex 200 10/300 column (GE Healthcare), previously equilibrated with buffer B. Samples enriched in the CML18 monomer were pooled, and sample quality was monitored by SDS–polyacrylamide gel electrophoresis. CML18 mutants D161N and W164A were purified following the same protocol.

Crystallization, data collection, structure solution, and refinement

Protein CML18 with 5 mM Ca^{2+} from purification was concentrated to 10 mg/ml and used for crystallization at 291 K with commercial matrix screens using the sitting drop vapor diffusion technique.

CSI&II condition F4 [0.1 M sodium citrate (pH 5.6), 0.5 M NaCl, and 2% v/v polyethylene imine] yielded small, cubic-shaped crystals that diffracted to around 7 Å. They were optimized by using additives in a 2:1:0.5 protein:screen:additive ratio, obtaining small almond-shaped crystals with 50% 1,4-dioxane. These crystals were cryoprotected using 25% glycerol and flash-frozen in liquid nitrogen, and diffraction data were collected at the BL13-Xaloc beamline in ALBA. This time, crystals diffracted to a 2.8-Å resolution.

Data processing

Diffraction data were indexed, integrated, and scaled using XDS (60) and AIMLESS from the CCP4 package (61). The structure of CML18 was solved by molecular replacement with Phaser (62) from the Phenix suite of programs (63) using the coordinates of the C-terminal domain of 4BYA and the N-terminal domain of 1QS7 as models. The quality of the maps and their predictive accuracy were greatly enhanced by the application of an anisotropic cutoff of the merged intensities using STARANISO (64). Hence, we used these data in subsequent refinement steps. The resolution limits of the refinement were determined using PAIREF (65). Structure building and successive cycles of refinement were carried out using Phenix Refine (63) and Coot (66). The protein cartoon figures were produced using Pymol (Molecular Graphics System, Schrödinger LLC). A summary of the data collection and refinement statistics is given in table S1.

Thermal-coupled intrinsic fluorescence

Protein CML18 was dialyzed against buffers containing either 20 mM MES (pH 6.3), 80 mM KCl, 5 mM NaCl, and 2 mM DTT (buffer C) with 20 mM EGTA or 20 mM tris (pH 8.3), 80 mM KCl, 5 mM NaCl, and 2 mM DTT (buffer D) with 20 mM EGTA. CML18 was dialyzed again against buffer C or D to remove EGTA.

To test the Ca^{2+} -sensing capabilities of CML18, the decalcified protein was titrated against increasing amounts of calcium using a Tycho instrument (NanoTemper Technologies). A constant concentration of 20 µM EGTA was maintained to neutralize free Ca^{2+} in water. Ten microliters of 25 µM CML18 was loaded into UV capillaries, and experiments were carried out by increasing the temperature at a rate of 20°C/min from 35° to 95°C. The initial fluorescence ratio was recorded by measuring tryptophan fluorescence emission at both 330 and 350 nm at the beginning of the experiment. To assess conformational changes driven by pH, 10 µl of 25 µM CML18 dialyzed against buffer C or D was loaded into UV capillaries. Experiments were carried out as above. To analyze CML18 binding to the synthetic CBD peptide, 10 µl of CBD peptide dissolved to 250 µM in buffer C or D was titrated against increasing amounts of decalcified CML18-W164A in the same buffer. After a brief incubation, the mix was loaded into UV capillaries and experiments were carried out as described above.

Isothermal titration calorimetry

To determine Ca^{2+} -binding affinities, ITC experiments were performed on a MicroCal PEAQ-ITC instrument. In each experiment 2-µl injections of 4 mM $CaCl_2$ were made to a 200-µl sample cell containing 200 µM of decalcified CML18 dialyzed to buffer C or D. Experiments were performed at 25°C with injections at 150-s intervals and 750-rpm stirring speed. Control experiments (injecting ligand solutions into the buffer) were conducted to obtain a baseline for each experiment and determine the heat of dilution/mixing. These values were subtracted from the experimental runs in the presence of protein. Analysis of the data was performed using the PEAQ-ITC analysis program. Two titrations were performed for two independent protein preparations.

Calorimetric titration of CBD peptide with CML18 was performed by the addition of 200 µM CML18 to a solution of 20 µM CBD peptide at 25°C in the presence of either 18 µM EGTA or 180 µM Ca^{2+} . Experimental details were identical to the ones expressed above.

Circular dichroism

All CD spectra were measured using a Jasco J-810 spectropolarimeter equipped with a computer-controlled Peltier device. Samples containing decalcified proteins CML18, CML18-D161N, or CML18-W164A (0.2 mg/ml) were measured in the far-UV region (320 to 202 nm) at 20°C in the presence of EGTA or $CaCl_2$. Quartz cuvettes with cell lengths of 1.0 mm were used.

For CD spectra of the CML18:CML-BD complex, a 1:1 ratio of protein:peptide at pH 6.3 and 8.3 was used. Experiments were carried out using the same equipment mentioned above.

Mutagenesis

To generate point mutation alleles, two different strategies were followed using the pBluescript (KS)-NHX1 plasmid as a template. For the first set of mutants, the NewEngland Biolabs' Q5 Site-Directed Mutagenesis Kit was used, following the manufacturer's specifications. The second set was obtained using a high-fidelity polymerase

and the following protocol (67). Primers (5' and 3') for these reactions were designed such that they had the desired mutation flanked by 10 base pairs fitting the template, and the reverse primer was the reverse complementary sequence of the forward primer. PCR reactions were performed with the Velocity DNA Polymerase kit (Bioline, London, UK). PCR amplicons were treated with *DpnI*, which cuts only the methylated GATC sites. To generate deletions in *NHX1*, mutagenesis by overlapping extension was performed. For functional tests in yeast, WT and mutant alleles were cloned in a plasmid derived from pDRI95 that tagged proteins at the C termini with HexaHis epitope. The expression of all protein variants was confirmed by Western blotting using antibodies Penta-His HRP Conjugate Qiagen 34460 at 1:2000 dilution (fig. S11).

Yeast methods

Yeast transformations were performed using the lithium acetate/polyethylene glycol method (68). Complementation assays were done with the yeast strain AXT3K (Δ ena1::HIS3::ena4, Δ nha1::LEU2, and Δ nhx1::KanMX4) (25) in which the *nhx1* mutation yields HygB sensitivity. Yeast cells were transformed with the *NHX1* allele clones in vector pDRI95 and selected in YNB without histidine and uracil. Yeast transformants were inoculated in 2 ml of YNB media supplemented with the corresponding amino acids and grown at 30°C overnight. The cells were then harvested and resuspended to a final OD₆₀₀ (optical density at 600 nm) of 0.5. Five microliters of serial decimal dilutions in water was spotted onto selective YPD plates supplemented with different concentrations of HygB and incubated at 30°C for 3 to 5 days. For growth measurement in liquid media, cultures were grown as above, and 20 μ l was used to inoculate a 96-well plate containing 200 μ l of liquid media per well. From the first well, 10-fold serial dilutions were made. Plates were incubated at 30°C and OD₆₀₀ in every well was measured at 24 and 48 hours with a Varioskan LUX Multimode Microplate Reader (Thermo Fisher Scientific). Three independent transformants for each construct were used in the assays. A detailed protocol for the determination of vacuolar pH in yeast has been described elsewhere (24).

For Y2Hs, cDNA fragments encoding the NHX1 to NHX4 C termini were subcloned in the pGBKT7-BD vector (Clontech). *CML17* and *CML18* cDNA were cloned in the pGADT7-AD vector (Clontech). The yeast strain AH109 was cotransformed with all combinations of pGADT7-AD and pGBKT7-BD constructs. Transformed colonies were selected in YNB-Trp-Leu plates and grown in 2 ml of YNB-Trp-Leu at 28°C until saturation (OD₆₀₀ ~ 2). From the saturated cultures, 1:10 serial dilutions were made and a 5- μ l drop of each dilution was plated onto YNB-Trp-Leu, YNB-His-Trp-Leu, and YNB-Ade-Trp-Leu plates for the selection of interactors. Plates were incubated at 28°C for 3 to 4 days. The split-ubiquitin assay for domain interaction was done according to (69). The pore domain of NHX1 (TM1 to TM9; residues M1 to T292) was fused to Cub-PLV in vector pMetYCgate. The CML18-binding domain (CBD; S486 to G516) or the cytosolic stretch between TM13 and the CBD (Loop, L453 to N480) were fused to NubG in vector pNXgate32. The channel KAT1 was used as a positive control for dimerization and as a negative control against NHX1-CBD. Double-transformed cultures were spotted in YNB plates with and without adenine and histidine for the selection of protein interaction. The expression of noninteracting proteins was confirmed by Western blotting using the HA and c-Myc tags provided by Y2H vectors (fig. S11). Antibodies were HA-Tag

Polyclonal Antibody, HRP conjugate (Invitrogen, PA1-29751) and c-Myc Monoclonal Antibody (9E10), HRP conjugate (Invitrogen, MA1-980-HRP).

Split-nanoluciferase assay

We developed vectors for a nLuc reconstitution assay in yeast. To allow in vivo cloning, the attB1-KanMX-attB2 cassette of pNXgate32-HA (70) was amplified by PCR with primers attB1_fwd (5'-CTC-GAGACAAGTTTGTACAAAAAAGCAGGCT) and attB2GSG_rev (5'-GCCGCTTCCGCCTCCGCCGCTGCCACCACCAAC-CACCTTTGTA). The DNA encoding the nLN was amplified by PCR with primers attB2GSG_fwd (5'-TACAAAGTGGTTGGTGGTG-GCAGCGCGGAGGCGGAAGCGGC) and HA2x_rev (5'-GACGT-CAAGCGTAGTCTGGAACGTCGTATGGGTAAC) using the vector HBT-nLucN-HA (71) as a template. The coding sequence of the nLC was amplified with primers attB2GSG_fwd and FLAG2x_rev (5'-GACAAGGACTACAAGGACGACGATGACAAGTGACGTC) using the vector HBT-nLucC-FLAG (71) as a template. The PCR fragment containing the attB1-KanMX-attB2 cassette was fused to the nLucN by overlapping PCR using the primers attB1_fwd and HA2x_rev. The final PCR product was digested with *XhoI/AatII* and cloned in the yeast shuttle vector pDEST32 (Invitrogen) cleaved with the same restriction enzymes; the resulting construct was named p32nLucNgate. In the same way, the attB1-KanMX-attB2 cassette was fused to the nLucN with primers attB1_fwd and FLAG2x_rev and cloned in pDEST22 (Invitrogen) producing the plasmid p22nLucCgate. Next, a fragment corresponding to TM9 (residues M263 to T292) was fused to the large nLN moiety of nLuc, whereas the CBD (residues S486 to G516) was fused to the smaller fragment nLC. A negative control construct with residues L453 to N480 comprising the protein stretch separating the CBD and the pore domain was fused to nLN. Plasmids were used to transform the W303 strain of *S. cerevisiae* (*MATa ura3-1 leu2-3,112 his3-11,15 trp1-1 ade2-1 can1-100*). Cells of overnight yeast cultures were grown for 3 to 4 hours in fresh medium to 0.5 OD_{600nm}, after which 90 μ l of samples were mixed with 10 μ l of Nano-Glo Luciferase Assay System reagent (Promega, Madison WI). Luminescence was measured after 5 min using a Varioskan LUX Multimode Microplate Reader (Thermo Fisher Scientific).

Plant materials and methods

T-DNA insertion lines SALK_069855 (*At1g32250*, *cml17*) and SALK_033749 (*At3g03000*, *cml18*) were obtained from ABRC. The genotype and insertion sites were confirmed by diagnostic PCR and sequencing of the amplicons. The *cml17 cml18* double mutant was obtained by crossing. The absence of *CML17* and *CML18* transcripts was assessed by RT-PCR.

Seeds were sterilized, stratified for 2 days at 4°C, and then placed onto rockwool in hydroponic culture with aerated nutrient solution [LAK medium, 1 mM KH₂PO₄, 2 mM Ca(NO₃)₂, 1 mM MgSO₄, 30 μ M H₃BO₃, 10 μ M MnSO₄, 1 μ M ZnSO₄, 1 μ M CuSO₄, 0.03 μ M (NH₄)₆Mo₇O₂₄, and 100 μ M Fe²⁺ as Sequestrene 138 Fe, pH ~5.3] (5). The LAK medium is specifically formulated to contain trace amounts of sodium and potassium. Salts (KCl and K₂SO₄) were added in 10 mM steps daily until reaching the K⁺ concentration indicated in each experiment. Treatments lasted 2 weeks, and the medium was changed weekly. Environmental controlled conditions were 16-hour light/8-hour dark, 80 to 100 μ M m⁻² s⁻¹, 23°C. For mineral analyses, shoots and roots were collected separately, washed with 10 mM MES

(pH 6.5), blotted dry, weighted individually, and frozen until use. Frozen tissues were ground and centrifuged to collect the cell sap that was submitted to flame emission photometry to determine their K^+ content.

Bimolecular fluorescence complementation

All vectors used have been described (72). cDNAs of *AtNHX1* and *AtNHX2* were subcloned in frame with the C-terminal moiety of enhanced yellow fluorescent protein (eYFP) in plasmid pSPYCE(M), and *AtCML18* was subcloned in vector pSPYNE(R)173 fused to the N-terminal segment of the eYFP protein. *Agrobacterium tumefaciens* strain GV3101 was transformed with BiFC constructs. The bacterial transformants were infiltrated in 5- to 6-week-old *N. benthamiana* leaves together with the p19-transformed *Agrobacterium* strain. The lower epidermis was inspected in a FluoView FV1000 fluorescence confocal microscope (Olympus) using a 515-nm laser and a 60× objective. Microscopy images were obtained using constant imaging conditions: exposure time of 1 ms for bright field and 1.2 s for UV light, a gain of 100, without offset, and 1 of binning. eYFP/C/eYFPN complexes were visualized using a YFP filter. Images were processed with Fiji software (73).

In planta pH and Ca^{2+} measurements

Col-0 plants expressing R-GECO1- E^2 GFP (42) were grown vertically in LAK-MES (pH 5.6) media [1 mM KH_2PO_4 , 2 mM $Ca(NO_3)_2$, 1 mM $MgSO_4$, 30 μ M H_3BO_3 , 10 μ M $MnSO_4$, 1 μ M $ZnSO_4$, 1 μ M $CuSO_4$, 0.03 μ M $(NH_4)_6Mo_7O_{24}$, 50 μ M FeNaEDTA, and 10 mM MES-tris (pH 5.6)] with 0.8% phytoagar. Four-day-old seedlings were transferred to imaging buffer [5 mM KCl, 50 μ M $CaCl_2$, and 10 mM MES-tris (pH 5.6)] during 15-min preincubation, and then transferred to the different treatments. After the 20-min incubation, one single image was taken of the root of each seedling using a Leica SP5II confocal laser scanning microscope with 10× air objective and photomultiplier tube detectors. The wavelengths for reporter excitation (and emission) were 561 nm (λ_{em} 580 to 640) for R-GECO1 and 458 nm (λ_{em} 510 to 550) and 488 nm (λ_{em} 510 to 550) for E^2 GFP. Image processing and analysis were conducted using Fiji (73). Image processing included background subtraction (2), Gaussian blur (1), median (1), 32-bit conversion, thresholding of background noise (0.002 for 561-nm R-GECO1 channel, 1 for 458- and 488-nm E^2 GFP channels), and ratio image calculation for E^2 GFP. Fluorescence emissions (F) and emission ratios (R) were measured as the average of all x-axis pixel values within the ROI comprising the region where the major changes of R were observed (455 μ m upward from the quiescent center). pH values were obtained from R values using a calibration curve. For the calibration curve, buffers between pH 5 and 9 were prepared according to (74).

Supplementary Materials

The PDF file includes:

Figs. S1 to S11
Tables S1 to S3
Legend for data S1

Other Supplementary Material for this manuscript includes the following:

Data S1

REFERENCES AND NOTES

1. S. Chanroj, G. Wang, K. Venema, M. W. Zhang, C. F. Delwiche, H. Sze, Conserved and diversified gene families of monovalent cation/ H^+ antiporters from algae to flowering plants. *Front. Plant Sci.* **3**, 25 (2012).
2. J. M. Pardo, B. Cubero, E. O. Leidi, F. J. Quintero, Alkali cation exchangers: Roles in cellular homeostasis and stress tolerance. *J. Exp. Bot.* **57**, 1181–1199 (2006).
3. S. V. Isayenkov, S. A. Dabravolski, T. Pan, S. Shabala, Phylogenetic diversity and physiological roles of plant monovalent cation/ H^+ antiporters. *Front. Plant Sci.* **11**, 573564 (2020).
4. K. Venema, F. J. Quintero, J. M. Pardo, J. P. Donaire, The *Arabidopsis* Na^+/H^+ exchanger AtNHX1 catalyzes low affinity Na^+ and K^+ transport in reconstituted liposomes. *J. Biol. Chem.* **277**, 2413–2418 (2002).
5. V. Barragan, E. Leidi, Z. Andres, L. Rubio, A. De Luca, J. Fernandez, B. Cubero, J. Pardo, Ion exchangers NHX1 and NHX2 mediate active potassium uptake into vacuoles to regulate cell turgor and stomatal function in *Arabidopsis*. *Plant Cell* **24**, 1127–1142 (2012).
6. E. Bassil, S. Zhang, H. Gong, H. Tajima, E. Blumwald, Cation specificity of vacuolar NHX-type cation/ H^+ antiporters. *Plant Physiol.* **179**, 616–629 (2019).
7. X.-Y. Jiang, E. O. Leidi, J. M. Pardo, How do vacuolar NHX exchangers function in plant salt tolerance? *Plant Signal Behav.* **5**, 792–795 (2010).
8. K. Venema, A. Belver, M. C. Marin-Manzano, M. P. Rodriguez-Rosales, J. P. Donaire, A novel intracellular K^+/H^+ antiporter related to Na^+/H^+ antiporters is important for K^+ ion homeostasis in plants. *J. Biol. Chem.* **278**, 22453–22459 (2003).
9. Q. S. Qiu, Y. Guo, M. A. Dietrich, K. S. Schumaker, J. K. Zhu, Regulation of SOS1, a plasma membrane Na^+/H^+ exchanger in *Arabidopsis thaliana*, by SOS2 and SOS3. *Proc. Natl. Acad. Sci. U.S.A.* **99**, 8436–8441 (2002).
10. H. Z. Shi, F. J. Quintero, J. M. Pardo, J. K. Zhu, The putative plasma membrane Na^+/H^+ antiporter SOS1 controls long-distance Na^+ transport in plants. *Plant Cell* **14**, 465–477 (2002).
11. F. J. Quintero, M. Ohta, H. Z. Shi, J. K. Zhu, J. M. Pardo, Reconstitution in yeast of the *Arabidopsis* SOS signaling pathway for Na^+ homeostasis. *Proc. Natl. Acad. Sci. U.S.A.* **99**, 9061–9066 (2002).
12. R. An, Q. J. Chen, M. F. Chai, P. L. Lu, Z. Su, Z. X. Qin, J. Chen, X. C. Wang, AtNHX8, a member of the monovalent cation : Proton antiporter-1 family in *Arabidopsis thaliana*, encodes a putative Li^+/H^+ antiporter. *Plant J.* **49**, 718–728 (2007).
13. S.-A. Whiteman, L. Serazetdinova, A. M. E. Jones, D. Sanders, J. Rathjen, S. C. Peck, F. J. M. Maathuis, Identification of novel proteins and phosphorylation sites in a tonoplast enriched membrane fraction of *Arabidopsis thaliana*. *Proteomics* **8**, 3536–3547 (2008).
14. M.-H. Sun, Q.-J. Ma, D.-G. Hu, X.-P. Zhu, C.-X. You, H.-R. Shu, Y.-J. Hao, The glucose sensor MdHXK1 phosphorylates a tonoplast Na^+/H^+ exchanger to improve salt tolerance. *Plant Physiol.* **176**, 2977–2990 (2018).
15. T. Yamaguchi, G. S. Aharon, J. B. Sottosanto, E. Blumwald, Vacuolar Na^+/H^+ antiporter cation selectivity is regulated by calmodulin from within the vacuole in a Ca^{2+} - and pH-dependent manner. *Proc. Natl. Acad. Sci. U.S.A.* **102**, 16107–16112 (2005).
16. I. C. M. Pabuayan, J. Jiang, H. Qian, J.-S. Chung, H. Shi, Gain-of-function mutations of AtNHX1 suppress *sos1* salt sensitivity and improve salt tolerance in *Arabidopsis*. *Stress Biol.* **1**, 14 (2021).
17. E. Bassil, H. Tajima, Y. C. Liang, M. A. Ohto, K. Ushijima, R. Nakano, T. Esumi, A. Coku, M. Belmonte, E. Blumwald, The *Arabidopsis* Na^+/H^+ antiporters NHX1 and NHX2 control vacuolar pH and K^+ homeostasis to regulate growth, flower development, and reproduction. *Plant Cell* **23**, 3482–3497 (2011).
18. Z. Andrés, J. Pérez-Hormaeche, E. O. Leidi, K. Schlücking, L. Steinhorst, D. H. McLachlan, K. Schumacher, A. M. Hetherington, J. Kudla, B. Cubero, J. M. Pardo, Control of vacuolar dynamics and regulation of stomatal aperture by tonoplast potassium uptake. *Proc. Natl. Acad. Sci. U.S.A.* **111**, E1806–E1814 (2014).
19. M. Reguera, E. Bassil, H. Tajima, M. Wimmer, A. Chanoca, M. S. Otegui, N. Paris, E. Blumwald, pH regulation by NHX-type antiporters is required for receptor-mediated protein trafficking to the vacuole in *Arabidopsis*. *Plant Cell* **27**, 1200–1217 (2015).
20. H. Sze, S. Chanroj, Plant endomembrane dynamics: Studies of K^+/H^+ antiporters provide insights on the effects of pH and ion homeostasis. *Plant Physiol.* **177**, 875–895 (2018).
21. K. Li, C. Gauschopf, R. Hedrich, I. Dreyer, K. R. Konrad, K^+ and pH homeostasis in plant cells is controlled by a synchronized K^+/H^+ antiport at the plasma and vacuolar membrane. *New Phytol.* **241**, 1525–1542 (2024).
22. S. Huang, L. Shen, M. R. G. Roelfsema, D. Becker, R. Hedrich, Light-gated channelrhodopsin sparks proton-induced calcium release in guard cells. *Science* **382**, 1314–1318 (2023).
23. K. Hamaji, M. Nagira, K. Yoshida, M. Ohnishi, Y. Oda, T. Uemura, T. Goh, M. H. Sato, M. T. Morita, M. Tasaka, S. Hasezawa, A. Nakano, I. Hara-Nishimura, M. Maeshima, H. Fukaki, T. Mimura, Dynamic aspects of ion accumulation by vesicle traffic under salt stress in *Arabidopsis*. *Plant Cell Physiol.* **50**, 2023–2033 (2009).
24. B. Rombolá-Caldentey, I. Mendoza, F. J. Quintero, J. M. Pardo, Structure-guided identification of critical residues in the vacuolar cation/proton antiporter NHX1 from *Arabidopsis thaliana*. *Plants* **12**, 2778 (2023).
25. F. J. Quintero, M. R. Blatt, J. M. Pardo, Functional conservation between yeast and plant endosomal Na^+/H^+ antiporters. *FEBS Lett.* **471**, 224–228 (2000).
26. J. Jumper, R. Evans, A. Pritzel, T. Green, M. Figurnov, O. Ronneberger, K. Tunyasuvunakool, R. Bates, A. Židek, A. Potapenko, A. Bridgland, C. Meyer, S. A. A. Kohl, A. J. Ballard, A. Cowie,

- B. Romera-Paredes, S. Nikolov, R. Jain, J. Adler, T. Back, S. Petersen, D. Reiman, E. Clancy, M. Zielinski, M. Steinegger, M. Pacholska, T. Berghammer, S. Bodenstern, D. Silver, O. Vinyals, A. W. Senior, K. Kavukcuoglu, P. Kohli, D. Hassabis, Highly accurate protein structure prediction with AlphaFold. *Nature* **596**, 583–589 (2021).
27. J. Srivastava, D. L. Barber, M. P. Jacobson, Intracellular pH sensors: Design principles and functional significance. *Physiology (Bethesda, Md.)* **22**, 30–39 (2007).
 28. J. R. Casey, S. Grinstein, J. Orlowski, Sensors and regulators of intracellular pH. *Nat. Rev. Mol. Cell Biol.* **11**, 50–61 (2010).
 29. B. J. Pope, K. M. Zierler-Gould, R. Kühne, A. G. Weeds, L. J. Ball, Solution structure of human cofilin: Actin binding, pH-sensitivity, and relationship to actin-depolymerizing factor. *J. Biol. Chem.* **279**, 4840–4848 (2004).
 30. S. Tornroth-Horsefield, Y. Wang, K. Hedfalk, U. Johanson, M. Karlsson, E. Tajkhorshid, R. Neutze, P. Kjellbom, Structural mechanism of plant aquaporin gating. *Nature* **439**, 688–694 (2006).
 31. A. N. Thompson, D. J. Posson, P. V. Parsa, C. M. Nimigeon, Molecular mechanism of pH sensing in KcsA potassium channels. *Proc. Natl. Acad. Sci. U.S.A.* **105**, 6900–6905 (2008).
 32. R. Fritz, K. Stiasny, F. X. Heinz, Identification of specific histidines as pH sensors in flavivirus membrane fusion. *J. Cell Biol.* **183**, 353–361 (2008).
 33. H. Tidow, P. Nissen, Structural diversity of calmodulin binding to its target sites. *FEBS J.* **280**, 5551–5565 (2013).
 34. A. Villarreal, M. Tagliarola, G. Bernardo-Seisdedos, A. Alaimo, J. Agirre, A. Alberdi, C. Gomis-Perez, M. V. Soldovieri, P. Ambrosino, C. Malo, P. Areso, The ever changing moods of calmodulin: How structural plasticity entails transductional adaptability. *J. Mol. Biol.* **426**, 2717–2735 (2014).
 35. M. R. Blatt, C. L. Slayman, Role of “active” potassium transport in the regulation of cytoplasmic pH by nonanimal cells. *Proc. Natl. Acad. Sci. U.S.A.* **84**, 2737–2741 (1987).
 36. P. M. Bayley, S. R. Martin, The alpha-helical content of calmodulin is increased by solution conditions favouring protein crystallisation. *Biochim. Biophys. Acta* **1160**, 16–21 (1992).
 37. W. E. Meador, A. R. Means, F. A. Quiocho, Modulation of calmodulin plasticity in molecular recognition on the basis of x-ray structures. *Science* **262**, 1718–1721 (1993).
 38. J. R. Lakowicz, *Principles of Fluorescence Spectroscopy* (Springer, 2007).
 39. S. G. F. Rasmussen, A. D. Jensen, G. Liapakis, P. Ghanouni, J. A. Javitch, U. Gether, Mutation of a highly conserved aspartic acid in the β_2 adrenergic receptor: Constitutive activation, structural instability, and conformational rearrangement of transmembrane segment 6. *Mol. Pharmacol.* **56**, 175–184 (1999).
 40. B. Ranty, D. Aldon, J. P. Galaud, Plant calmodulins and calmodulin-related proteins: Multifaceted relays to decode calcium signals. *Plant Signal. Behav.* **1**, 96–104 (2006).
 41. T. J. Lane, Protein structure prediction has reached the single-structure frontier. *Nat. Methods* **20**, 170–173 (2023).
 42. R. Waadt, P. Köster, Z. Andrés, C. Waadt, G. Bradamante, K. Lampou, J. Kudla, K. Schumacher, Dual-reporting transcriptionally linked genetically encoded fluorescent indicators resolve the spatiotemporal coordination of cytosolic abscisic acid and second messenger dynamics in Arabidopsis. *Plant Cell* **32**, 2582–2601 (2020).
 43. F. L. Wang, Y. L. Tan, L. Wallrad, X. Q. Du, A. Eickelkamp, Z. F. Wang, G. F. He, F. Rehms, Z. Li, J. P. Han, I. Schmitz-Thom, W. H. Wu, J. Kudla, Y. Wang, A potassium-sensing niche in *Arabidopsis* roots orchestrates signaling and adaptation responses to maintain nutrient homeostasis. *Dev. Cell* **56**, 781–794.e6 (2021).
 44. E. O. Leidi, V. Barragan, L. Rubio, A. El-Hamdaoui, T. Ruiz, B. Cubero, J. A. Fernandez, R. A. Bressan, P. M. Hasegawa, F. J. Quintero, J. M. Pardo, The ATNHX1 exchanger mediates potassium compartmentation in vacuoles of transgenic tomato. *Plant J.* **61**, 495–506 (2010).
 45. Y. Wang, W. H. Wu, Regulation of potassium transport and signaling in plants. *Curr. Opin. Plant Biol.* **39**, 123–128 (2017).
 46. P. Ragel, N. Raddatz, E. O. Leidi, F. J. Quintero, J. M. Pardo, Regulation of K⁺ nutrition in plants. *Front. Plant Sci.* **10**, 281 (2019).
 47. T. C. de Bang, S. Husted, K. H. Laursen, D. P. Persson, J. K. Schjoerring, The molecular-physiological functions of mineral macronutrients and their consequences for deficiency symptoms in plants. *N. Phytol.* **229**, 2446–2469 (2021).
 48. J.-Y. Zhou, D.-L. Hao, G.-Z. Yang, Regulation of cytosolic pH: The contributions of plant plasma membrane H⁺-ATPases and multiple transporters. *Int. J. Mol. Sci.* **22**, 12998 (2021).
 49. C. Lee, H. J. Kang, C. von Ballmoos, S. Newstead, P. Uzdaviny, D. L. Dotson, S. Iwata, O. Beckstein, A. D. Cameron, D. Drew, A two-domain elevator mechanism for sodium/proton antiport. *Nature* **501**, 573–577 (2013).
 50. I. Winklemann, R. Matsuoka, P. F. Meier, D. Shutin, C. Zhang, L. Orellana, R. Sexton, M. Landreh, C. V. Robinson, O. Beckstein, D. Drew, Structure and elevator mechanism of the mammalian sodium/proton exchanger NHE9. *EMBO J.* **39**, e105908 (2020).
 51. Y. Zhang, J. Zhou, X. Ni, Q. Wang, Y. Jia, X. Xu, H. Wu, P. Fu, H. Wen, Y. Guo, G. Yang, Structural basis for the activity regulation of Salt Overly Sensitive 1 in *Arabidopsis* salt tolerance. *Nat. Plants* **9**, 1915–1923 (2023).
 52. Y. Dong, Y. Gao, A. Ilie, D. Kim, A. Boucher, B. Li, X. C. Zhang, J. Orlowski, Y. Zhao, Structure and mechanism of the human NHE1-CHP1 complex. *Nat. Commun.* **12**, 3474 (2021).
 53. M. Trande, M. Pedretti, M. C. Bonza, A. Di Matteo, M. D’Onofrio, P. Dominici, A. Astegno, Cation and peptide binding properties of CML7, a calmodulin-like protein from *Arabidopsis thaliana*. *J. Inorg. Biochem.* **199**, 110796 (2019).
 54. V. La Verde, M. Trande, M. D’Onofrio, P. Dominici, A. Astegno, Binding of calcium and target peptide to calmodulin-like protein CML19, the centrin 2 of *Arabidopsis thaliana*. *Int. J. Biol. Macromol.* **108**, 1289–1299 (2018).
 55. A. Ogunrinde, K. Munro, A. Davidson, M. Ubaid, W. A. Snedden, *Arabidopsis* calmodulin-like proteins, CML15 and CML16 possess biochemical properties distinct from calmodulin and show non-overlapping tissue expression patterns. *Front. Plant Sci.* **8**, 2175 (2017).
 56. A. Astegno, M. C. Bonza, R. Vallone, V. La Verde, M. D’Onofrio, L. Luoni, B. Molesini, P. Dominici, *Arabidopsis* calmodulin-like protein CML36 is a calcium (Ca²⁺) sensor that interacts with the plasma membrane Ca²⁺-ATPase isoform ACA8 and stimulates its activity. *J. Biol. Chem.* **292**, 15049–15061 (2017).
 57. R.-J. Tang, F.-G. Zhao, Y. Yang, C. Wang, K. Li, T. J. Kleist, P. G. Lemaux, S. Luan, A calcium signalling network activates vacuolar K⁺ remobilization to enable plant adaptation to low-K environments. *Nat. Plants* **6**, 384–393 (2020).
 58. F. J. M. Maathuis, Vacuolar two-pore K⁺ channels act as vacuolar osmosensors. *N. Phytol.* **181**, 84–91 (2011).
 59. A. Gobert, S. Isayenkov, C. Voelker, K. Czempinski, F. J. Maathuis, The two-pore channel TPK1 gene encodes the vacuolar K⁺ conductance and plays a role in K⁺ homeostasis. *Proc. Natl. Acad. Sci. U.S.A.* **104**, 10726–10731 (2007).
 60. W. Kabsch, XDS. *Acta Crystallogr. D. Biol. Crystallogr.* **66**, 125–132 (2010).
 61. M. D. Winn, C. C. Ballard, K. D. Cowtan, E. J. Dodson, P. Emsley, P. R. Evans, R. M. Keegan, E. B. Krissinel, A. G. Leslie, A. McCoy, S. J. McNicholas, G. N. Murshudov, N. S. Pannu, E. A. Potterton, H. R. Powell, R. J. Read, A. Vagin, K. S. Wilson, Overview of the CCP4 suite and current developments. *Acta Crystallogr. D. Biol. Crystallogr.* **67**, 235–242 (2011).
 62. A. J. McCoy, R. W. Grosse-Kunstleve, P. D. Adams, M. D. Winn, L. C. Storoni, R. J. Read, Phaser crystallographic software. *J. Appl. Crystallogr.* **40**, 658–674 (2007).
 63. P. D. Adams, P. V. Afonine, G. Bunkóczi, V. B. Chen, I. W. Davis, N. Echols, J. J. Headd, L. W. Hung, G. J. Kapral, R. W. Grosse-Kunstleve, A. J. McCoy, N. W. Moriarty, R. Oeffner, R. J. Read, D. C. Richardson, J. S. Richardson, T. C. Terwilliger, P. H. Zwart, PHENIX: A comprehensive Python-based system for macromolecular structure solution. *Acta Crystallogr. D. Biol. Crystallogr.* **66**, 213–221 (2010).
 64. C. Vornheim, I. J. Tickle, C. Flensburg, P. Keller, W. Paciorek, A. Sharff, G. Brice, Advances in automated data analysis and processing within autoPROC, combined with improved characterisation, mitigation and visualisation of the anisotropy of diffraction limits using STARANISO. *Acta Crystallogr. Sec. A* **74**, A360 (2018).
 65. M. Malý, K. Diederichs, J. Dohnálek, P. Kolenko, Paired refinement under the control of PAIRF. *IUCr J* **7**, 681–692 (2020).
 66. P. Emsley, K. Cowtan, Coot: Model-building tools for molecular graphics. *Acta Crystallogr. D. Biol. Crystallogr.* **60**, 2126–2132 (2004).
 67. W. Wang, B. A. Malcolm, Two-stage PCR protocol allowing introduction of multiple mutations, deletions and insertions using QuikChange™ site-directed mutagenesis. *Biotechniques* **26**, 680–682 (1999).
 68. R. Elble, A simple and efficient procedure for transformation of yeasts. *Biotechniques* **13**, 18–20 (1992).
 69. C. Grefen, P. Obrdlík, K. Harter, The determination of protein-protein interactions by the mating-based split-ubiquitin system (mbSUS). *Methods Mol. Biol.* **479**, 217–233 (2009).
 70. P. Obrdlík, M. El-Bakkoury, T. Hamacher, C. Cappellaro, C. Vilarino, C. Fleischer, H. Ellerbrok, R. Kamuzinzi, V. Ledent, D. Blaudez, D. Sanders, J. L. Revuelta, E. Boles, B. Andre, W. B. Frommer, K⁺ channel interactions detected by a genetic system optimized for systematic studies of membrane protein interactions. *Proc. Natl. Acad. Sci. U.S.A.* **101**, 12242–12247 (2004).
 71. F. Z. Wang, N. Zhang, Y. J. Guo, B. Q. Gong, J. F. Li, Split Nano luciferase complementation for probing protein-protein interactions in plant cells. *J. Integr. Plant Biol.* **62**, 1065–1079 (2020).
 72. R. Waadt, L. K. Schmidt, M. Lohse, K. Hashimoto, R. Bock, J. Kudla, Multicolor bimolecular fluorescence complementation reveals simultaneous formation of alternative CBL/CIPK complexes in planta. *Plant J.* **56**, 505–516 (2008).
 73. J. Schindelin, I. Arganda-Carreras, E. Frise, V. Kaynig, M. Longair, T. Pietzsch, S. Preibisch, C. Rueden, S. Saalfeld, B. Schmid, J.-Y. Tinevez, D. J. White, V. Hartenstein, K. Eliceiri, P. Tomancak, A. Cardona, Fiji: An open-source platform for biological-image analysis. *Nat. Methods* **9**, 676–682 (2012).
 74. M. Krebs, D. Beyhl, E. Gorlich, K. A. Al-Rasheid, I. Marten, Y. D. Stierhof, R. Hedrich, K. Schumacher, *Arabidopsis* V-ATPase activity at the tonoplast is required for efficient nutrient storage but not for sodium accumulation. *Proc. Natl. Acad. Sci. U.S.A.* **107**, 3251–3256 (2010).

Acknowledgments: We are indebted to L. Lagartera, Service of Biophysical Interactions at the Instituto de Química Medica, CSIC, Madrid, for the ITC data. We also thank A. I. Lopez and L. Lopez-Maury (Institute of Plant Biochemistry and Photosynthesis) for assistance with Western

blots. **Funding:** This work was supported by the Agencia Estatal de Investigación of the Spanish Ministry of Science and Innovation (MCIN/AEI/10.13039/501100011033) with grants PID2020-119805RB-I00 (to A.A.I.) and PID2021-126863NB-I00 (to J.M.P.) cofinanced by "ERDF A way of making Europe". M.D.-M. was supported by grant PRE2018-083280 cofinanced by "ESF Investing in your future". P.R. was supported by the Marie Skłodowska-Curie action H2020-MSCA-IF-2017-786459. **Author contributions:** Conceptualization: F.J.Q., A.A.I., and J.M.P. Data acquisition: M.D.-M., B.R.-C., I.M., P.R., A.d.L., R.C., A.M.A., A.Au., and B.C. Data analysis and supervision: K.S., F.J.Q., A.A.I., and J.M.P. Funding acquisition and project administration: A.A.I. and J.M.P. Writing: A.A.I. and J.M.P. **Competing interests:** The authors declare that they

have no competing interests. **Data and materials availability:** All data needed to evaluate the conclusions in the paper are present in the paper and/or the Supplementary Materials. The atomic coordinates and structure factors of CML18 have been deposited in the Protein Data Bank (www.wwpdb.org) with PDB ID: 8RX8.

Submitted 10 April 2024

Accepted 8 October 2024

Published 13 November 2024

10.1126/sciadv.adp7658